Review Article

ADVANCED PHOTONICS

Advances in metal halide perovskite lasers: synthetic strategies, morphology control, and lasing emission

Zhiping Hu,[a] Zhengzheng Liu,[b] Zijun Zhan,[a] Tongchao Shi,[b] Juan Du,[a,b,*] Xiaosheng Tang,[c,d,*] and Yuxin Leng[a,b,*]

[a]University of Chinese Academy of Sciences, Hangzhou Institute for Advanced Study, Hangzhou, China
[b]Chinese Academy of Sciences, Shanghai Institute of Optics and Fine Mechanics, State Key Laboratory of High Field Laser Physics and CAS Center for Excellence in Ultra-Intense Laser Science, Shanghai, China
[c]Chongqing University of Posts and Telecommunications, School of Optoelectronic Engineering, Chongqing, China
[d]Zhengzhou University, School of Materials Science and Engineering, Zhengzhou, China

Abstract. In the past decade, lead halide perovskites have emerged as potential optoelectronic materials in the fields of light-emitting diode, solar cell, photodetector, and laser, due to their low-cost synthesis method, tunable bandgap, high quantum yield, large absorption, gain coefficient, and low trap-state densities. In this review, we present a comprehensive discussion of lead halide perovskite applications, with an emphasis on recent advances in synthetic strategies, morphology control, and lasing performance. In particular, the synthetic strategies of solution and vapor progress and the morphology control of perovskite nanocrystals are reviewed. Furthermore, we systematically discuss the latest development of perovskite laser with various fundamental performances, which are highly dependent on the dimension and size of nanocrystals. Finally, considering current challenges and perspectives on the development of lead halide perovskite nanocrystals, we provide an outlook on achieving high-quality lead perovskite lasers and expanding their practical applications.

Keywords: perovskite; nanocrystal; morphology; stimulated emission; laser.

Received Jan. 8, 2021; revised manuscript received Apr. 13, 2021; accepted for publication Apr. 27, 2021; published online Jun. 2, 2021.

[DOI: 10.1117/1.AP.3.3.034002]

1 Introduction

Research related to perovskites can be traced back to 1970s,[1–3] but systematic research was lacking due to technology limitations in that period. In 2009, Kojima et al.[4] first added organic–inorganic hybrid perovskites as semiconductor materials in dye-sensitized solar cells, achieving a power conversion efficiency (PCE) of 3.8%. Since that breakthrough, the development of perovskites with large absorption coefficient, low defect state density, long carrier diffusion length, and bipolar carrier transport property has made them uniquely suitable for photovoltaic applications.[4–16] Currently, the PCE of single-junction pure perovskite-based solar cells has reached 25.5% for small-area devices and 24.2% for large area over 1 cm^2.[15,17] According to the Shockley–Queisser limit, a type of high-quality conversion material in solar cells is also efficient luminescent materials in light-emitting devices such as LEDs and lasers.[18–20] In 2004, the first evidence of optical gain in lead halide perovskites was reported, which is amplified spontaneous emission (ASE) from microcrystalline films of $CsPbCl_3$ recrystallized from the amorphous phase.[21,22] In 2014, ASE and lasing were realized from $MAPbX_3$ polycrystalline thin films at room temperature. Ultralow threshold could benefit from the excellent optical absorption of $MAPbX_3$ with a coefficient greater than 2×10^4 cm^{-1}.[23–27]

In addition, the research about micro/nanolasers based on perovskite with high coherence, low threshold, and high-quality factor has increased rapidly. The advances in lasing performance mainly benefit from the excellent optical properties such as high photoluminescence quantum yield (PLQY), narrow linewidth, large absorption coefficient, and widely tuned band.[28–32] In addition, the shape and size of perovskite could be flexibly adjusted, which can affect their physical and chemical properties and the performance of optoelectrical devices.[33–36] Hence, various

*Address all correspondence to Xiaosheng Tang, xstang@cqu.edu.cn; Juan Du, dujuan@mail.siom.ac.cn; Yuxin Leng, lengyuxin@mail.siom.ac.cn

synthesis strategies about the fabrication, control of morphologies, and sizes of perovskite nanocrystals (NCs) have been developed. The size can be adjusted from several nanometers to microns, and the morphologies can be controlled as zero-dimension (0D) quantum dots (QDs), one-dimensional (1D) nanorods (NRs) and nanowires (NWs), two-dimensional (2D) nanoplates (NPs) and nanosheets (NSs), and three-dimensional (3D) nanocubes and microspheres (MSs).[37–42] In this review, we discuss and summarize the recent developments in lead halide perovskite materials and perovskite-based lasers. In particular, the synthetic strategies of the perovskite containing solution process and vapor evaporation method are reviewed. Moreover, the morphology control of perovskite with various dimensions for the natural resonant cavities of lasing is discussed. Based on the perovskite QDs, NWs, NRs, NPs, and MSs, the single perovskite nano/microlaser and laser array are reviewed, and the dependence of laser performance on structure morphology is discussed. Finally, we present a summary and the perspectives of future research in the perovskite-based laser.

2 Morphology Control of Perovskite NCs

2.1 Structure of Perovskite

As a kind of chemical material with an ABX_3-type structure [Fig. 1(a)], the crystal structure of perovskite is the same as calcium titanate ($CaTiO_3$).[43] "A" could be an organic molecular group such as methylamino (MA) or an inorganic element such as cesium (Cs); "B" is generally a metal ion, such as lead (Pb), tin (Sn), and bismuth (Bi); "X" refers to a halide ion containing Cl, Br, and I. The tolerance factor (t) is generally used to evaluate the structural formability and stability, calculated as $t = (r_A + r_X)/\sqrt{2}(r_B + r_X)$, where r_A, r_B, and r_X are ionic radii of A, B, and X sites, respectively. Li et al.[45] introduced the "octahedral factor" (μ) to investigate the regularities of formability for cubic perovskite ABX_3, which was defined as $\mu = r_B/r_X$ and suggested the formation of the halide perovskites under the conditions of $0.813 < t < 1.107$ and $0.377 < \mu < 0.895$. Then, Sun et al. introduced $(t+\mu)^{\eta}$ to evaluate the thermodynamic stability of hailde perovskite, where η is the atomic packing fraction in a crystal structure. By calculating decomposition energies of 138 perovskite compounds [Fig. 1(b)], they demonstrated better accuracy of $(t+\mu)^{\eta}$ than the evaluation of t and μ alone.[44,46]

2.2 Perovskite Quantum Dots

Based on the ABX_3 halide perovskites, the morphologies can be controlled with different dimensional nanostructures, such as 0D QDs, 1D NWs, 2D NPs, and 3D MSs.[37,40,47–65] Since different nanostructures will result in variable structure–property relationships at the nanoscale level, various strategies have been reported for controlling the form and size of the perovskite NCs, including changing the reaction temperature, the reaction time, and the ligand combinations during synthesis.[37–42] In addition, capping ligands with different structures and lengths can also affect the nucleation and growth rate, hence the structure of perovskite NCs can be adjusted owing to their anchoring and steric effects.[47–49]

As is well known, traditional semiconductor QDs have a quantum size effect. In the case of perovskite QDs, the bandgap can also be tuned via halide component regulation.[38–42,51] Zhang et al.[25] developed a ligand-assisted reprecipitation (LARP) method to fabricate $MAPbBr_3$ QDs at room temperature. Their PLQYs were up to ~70% [Fig. 2(a)]. By mixing PbX_2 salts into

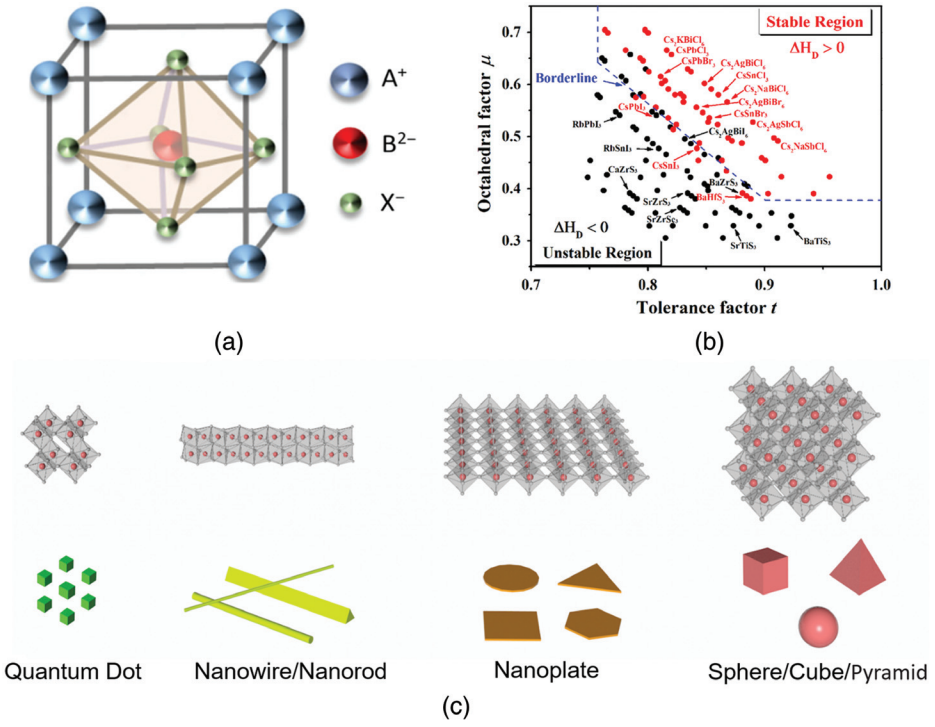

Fig. 1 (a) Structural model of metal lead perovskites. Figures reproduced from Ref. 43. (b) The (t,μ) map for 138 perovskite compounds. Figures reproduced from Ref. 44. (c) Nanoscale morphologies of halide perovskites.

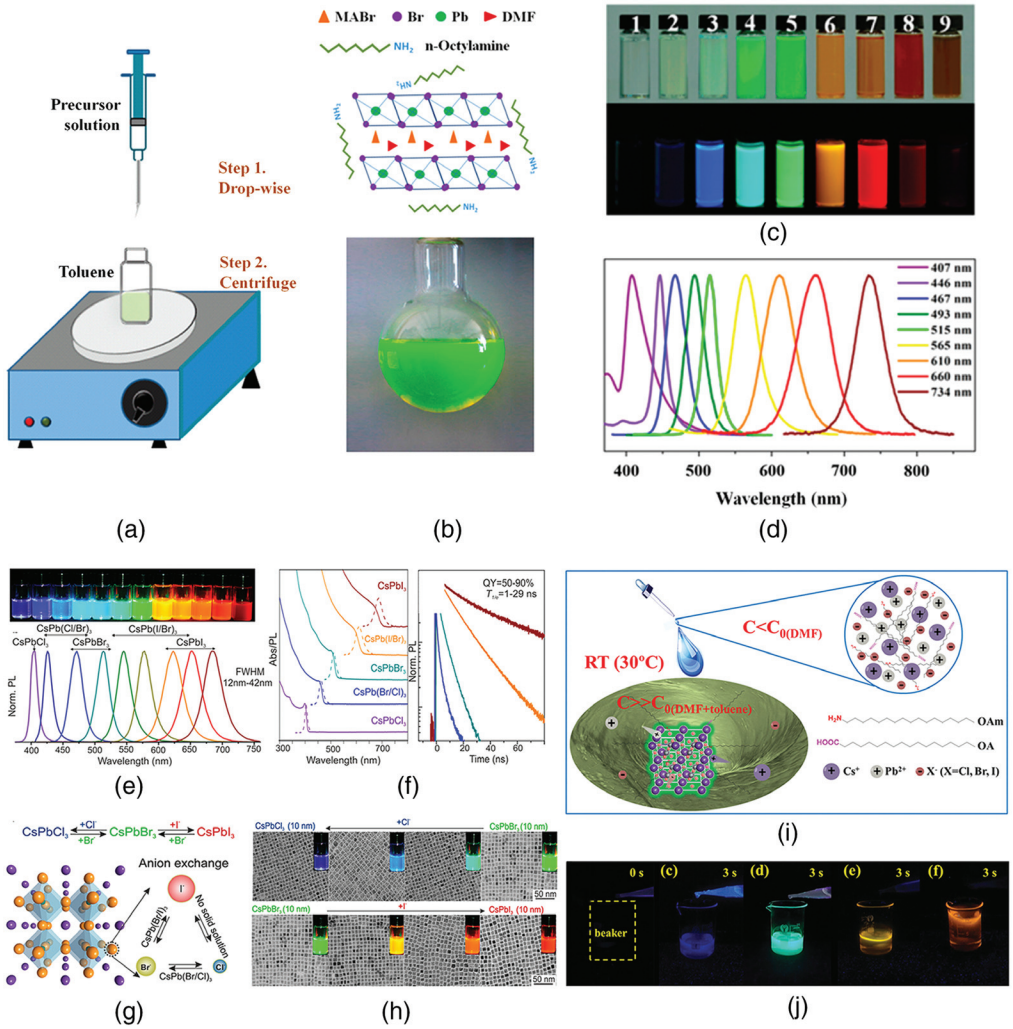

Fig. 2 (a) Schematic of LARP technique. Figures reproduced from Ref. 25. (b) Schematic of precursor and optical image of $MAPbBr_3$ solution. Figures reproduced from Ref. 25. (c) Optical images of $MAPbX_3$ solution under natural light and under 365 nm excitation. Figures reproduced from Ref. 25. (d) PL spectra of $MAPbX_3$ QDs. Figures reproduced from Ref. 25. (e) PL optical images and PL spectra of $CsPbX_3$ QDs. Figures reproduced from Ref. 42. (f) Time-resolved PL decays for $CsPbX_3$ QDs. Figures reproduced from Ref. 42. (g) Schematic of the anion-exchange of $CsPbX_3$. Figures reproduced from Ref. 41. (h) TEM images of $CsPbX_3$ QDs with various PL. Figures reproduced from Ref. 41. (i) Schematic of room-temperature fabrication of $CsPbX_3$ QDs. Figures reproduced from Ref. 39. (j) Optical images of $CsPbX_3$ QDs after the addition of precursor ion solutions for 3 s. Figures reproduced from Ref. 39.

the precursors, the authors tuned emission in the range of 407 to 734 nm [Figs. 2(c) and 2(d)].[25] In the case of all-inorganic ones, the emission spectra of $CsPbX_3$ QDs fabricated by the high temperature method could be tunable over 410 to 700 nm with narrow half maximum of 12 to 42 nm and radiative lifetime of 1 to 29 ns [Figs. 2(e) and 2(f)].[42] Subsequently, they proposed an anion-exchange process to tune the emission of colloidal $CsPbX_3$ QDs via postsynthetic reactions with different compounds [Figs. 2(g) and 2(h)].[41] Besides the hot-injection technique, the room-temperature synthesis for perovskite QDs was also studied.[39] In 2016, Zeng and coworkers developed a room-temperature method to fabricate $CsPbX_3$ QDs via supersaturated recrystallization. In this process, the crystallization process occurred in the transform of Cs^+, Pb^{2+}, and X^- ions from soluble to insoluble solvents in the absence of inert gas within a few seconds, as shown in Figs. 2(i) and 2(j).[39] Although crystallized at room temperature, these $CsPbX_3$ QDs held superior optical properties with PLQYs above 70%, and PLs can remain at ~90% after aging 30 days in the air. Except for being regulated by changing composition, the bandgap of perovskite QDs also can be tuned by the size regulation of QDs. Chen et al.[66] fabricated $CsPbBr_3$ QDs with an average diameter from 7.1 to 12.3 nm by modifying the temperature, and the corresponding PL emission peaks could be tuned from 493 to 531 nm. Fang et al.[67] synthesized $MAPbBr_3$ QDs with tunable average diameter from 2.82 to 5.29 nm by varying the additive amount of surfactant, and the corresponding PL emission peaks could shift from 436 to 520 nm due to the quantum confinement effect. Most recently, there have been much more researches about perovskite QDs by composition engineering for wider optoelectronic applications.[68–70]

2.3 Perovskite Nanowires and Nanorods

Perovskite 1D NWs and NRs are more applicable in the field of optoelectronic applications due to their special anisotropic structures. In the growth of 1D perovskite structures, reaction temperature, reaction time, and organic ligands are critical factors for crystallization.[71–74] Deng et al.[71] first fabricated $MAPbI_3$ NWs via the one-step solution method. In this process, the precursor solution containing PbI_2 and CH_3NH_3I was dropped onto a substrate and then heated at different temperatures. Finally, uniform $MAPbI_3$ NWs were obtained after heating at 80°C for 10 min. In 2017, they fabricated $Cs_x(MA)_{1-x}PbI_3$ NWs through a two-step solution method.[72] As shown in Fig. 3(a), PbI_2 powder was dissolved in water at 75°C initially, then PbI_2 separated out when the solution cooled down to room temperature. With the addition of CsI and MAI, perovskite NWs could be formed after shaking for a few seconds. The length and diameter of obtained perovskite NWs could reach 10 μm and several hundred nanometers. Moreover, the amount of perovskite NWs was related to the concentration of PbI_2 separated out from aqueous solution.[72] Zhu et al. developed a direct conversion of $MAPbI_3$ film into NWs through a recrystallization process [Fig. 3(b)]. The first step was the formation of perovskite film from a mixture of $PbCl_2$ and CH_3NH_3I.[73] Then, a mixture solution containing DMF and isopropyl was dropped onto the as-grown perovskite film. Along with the evaporation of the solvent, NWs could be formed [Fig. 3(b)].[73] Furthermore, they found the content of DMF in isopropyl, and the rotation speed could affect the sizes of prepared $MAPbI_3$ NWs.

As for all-inorganic perovskite, in 2015, Yang and coworkers used a solution method to synthesize single-crystalline $CsPbX_3$ NWs first. The reaction temperature was set as 150°C to 250°C.[51] They found that the reaction time was critical to the growth of NWs. As shown in Fig. 3(c), the SEM of prepared $CsPbBr_3$ with different reaction times showed perovskite nanocubes formed initially, then NS and NW formed at 90 min [Fig. 3(c)].[51] In the formation of Cs-based perovskite NWs, surface ligands could affect the width and size. Imran et al.[56] tuned the width of $CsPbX_3$ NWs from 10 to 20 nm by regulating the ratio of octylamine to oleylamine and varying the reaction time. They found that the width of NWs can be decreased below ~5 nm by introducing carboxylic acids with short aliphatic chains. Correspondingly, the emission spectra of $CsPbBr_3$ NWs could be tuned from 524 to 473 nm [Fig. 3(d)].[56] Amgar et al.[58] found that various hydrohalic acids (HX, X = Cl, Br, and I) affect the length of $CsPbBr_3$ NWs efficiently. With the increasing amount of HX, the length of NWs would be shortened [Fig. 3(e)]. Using this method, the emission of the $CsPbBr_3$ NWs could be tunable in the range of 423 to 505 nm [Fig. 3(f)].[58] $CsPbBr_3$ NWs/NRs can also be synthesized by a low-temperature method. Dong's group[74] fabricated $CsPbBr_3$ perovskite NRs with controllable size in a polymer matrix. Then, Liu et al. fabricated single-crystalline $CsPbBr_3$ NWs without inert gas at room temperature. By increasing the reaction time, the length of NWs could be increased from nanometers to micrometers, and the diameter could be tuned from 2.5 to 32.0 nm. Moreover, using this method, the emission spectra of $CsPbX_3$ NWs could be tuned from 434 to 681 nm.[57]

Besides the above-mentioned solution-process, plenty of works have been reported on synthesizing perovskite NWs and NRs by vapor-phase growth.[49] More than ever, the vapor-phase process can control the morphology and crystalline phase of perovskite NCs efficiently. It has been demonstrated that the growth temperature and the substrates are critical for the orientation of perovskite NWs in vapor-growth. Xing et al.[49] first used the vapor-phase technique to fabricate perovskite NWs. First, PbI_2 NWs were deposited on SiO_2 substrates by the chemical vapor deposition (CVD) method [Fig. 4(a)].[49] Consequently, PbI_2 was converted into $MAPbX_3$ after the reaction with MAX through a CVD process. As shown in Fig. 4(b), the prepared $MAPbI_3$ wires had a length about tens of micrometers and a diameter of ~500 nm. In Figs. 4(c) and 4(d), they indicated that $MAPbI_3$ NW grows along the [100] direction.[49] Due to the thermal decomposition of organic hybrid perovskite occurring easily at high temperatures, direct vapor–phase growth of hybrid perovskites is more challenging. However, the vapor–phase technique is an attractive method for all-inorganic perovskites, which have better thermostability. Zhou et al.[75] prepared $CsPbX_3$ NRs with high crystallization quality and regular triangular morphology through a vapor deposition method [Fig. 4(e)]. As shown in the SEM image [Fig. 4(f)], prepared $CsPbX_3$ NRs had a triangular cross section, smooth surfaces, and a length of 2 to 20 μm. They

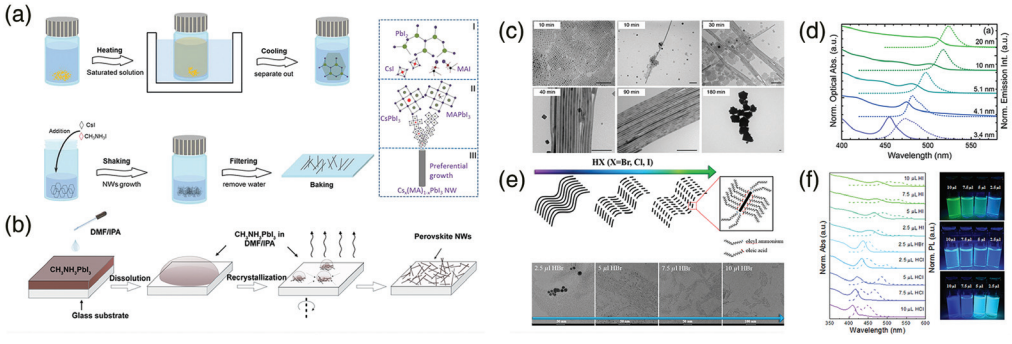

Fig. 3 (a) Schematic of the fabrication process for the $Cs_x(CH_3NH_3)_{1-x}PbI_3$ NWs. Figures reproduced from Ref. 72. (b) Schematic of the formation of the $MAPbI_3$ NWs by recrystallization process. Figures reproduced from Ref. 73. (c) TEM images of as-grown $CsPbBr_3$ NCs with increasing times. Figures reproduced from Ref. 51. (d) Absorption and PL spectra of $CsPbBr_3$ NWs. Figures reproduced from Ref. 56. (e) Schematic of the passivation effect by HX on the length of $CsPbX_3$ NWs and TEM images of the synthesized $CsPbX_3$ NWs. Figures reproduced from Ref. 58. (f) Normalized absorption, PL spectra, and photographs of $CsPbX_3$ NWs. Figures reproduced from Ref. 58.

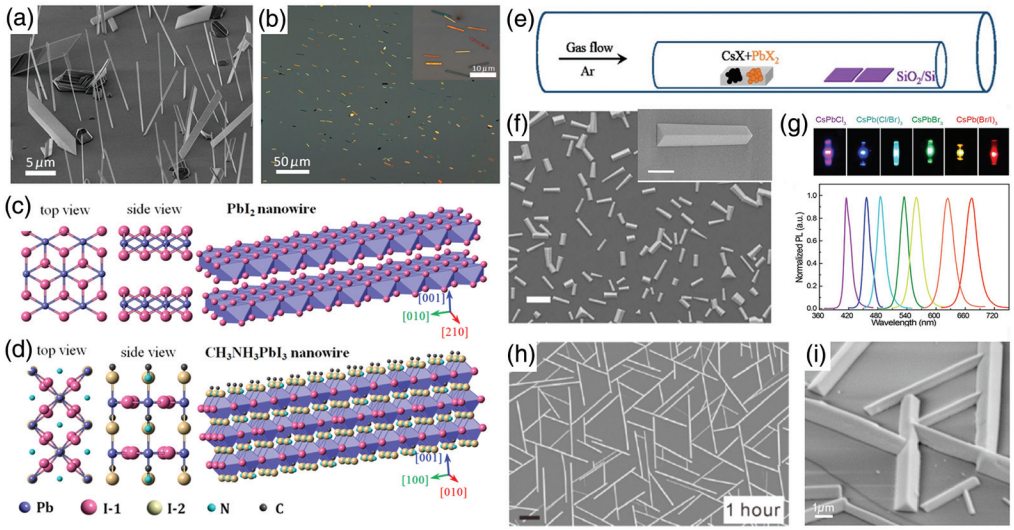

Fig. 4 (a) SEM image of PbI_2 NWs. Figures reproduced from Ref. 49. (b) Optical microscopy image of $MAPbI_3$ NWs. Figures reproduced from Ref. 49. Structure simulation images of (c) PbI_2 NW and (d) $MAPbI_3$ NW. Figures reproduced from Ref. 49. (e) Schematic of the $CsPbX_3$ triangular micro/NRs. Figures reproduced from Ref. 75. (f) SEM image of $CsPbBr_3$ triangular rods. Figures reproduced from Ref. 75. (g) Real-color image and PL spectra of $CsPbX_3$ triangular rods. Figures reproduced from Ref. 75. (h), (i) SEM images of the $CsPbBr_3$ NWs. Figures reproduced from Ref. 62.

demonstrated that the reaction temperature was critical for the control of perovskite NCs during the growth of triangular $CsPbBr_3$ NRs. Moreover, the emission of these as-grown $CsPbX_3$ NRs also can be tuned from 415 to 673 nm by halide component regulation [Fig. 4(g)].[75]

In addition, it has been confirmed that the substrate can affect the grain orientation growth of perovskite NWs.[76] Chen et al.[62] fabricated $CsPbX_3$ wires on mica by the CVD method. During the growth of $CsPbBr_3$ NWs, heteroepitaxial matching occurred in the interface between $CsPbBr_3$ NCs and mica substrate. Then, the formation of NWs was caused by the asymmetric lattice mismatch with the mica substrate. As shown in Figs. 4(h) and 4(i), the obtained $CsPbBr_3$ wires were well-aligned, surface-bound, and formed a network with a length about tens of μm and width of $\sim$1 μm, respectively.[62] Moreover, various nanostructures could be formed by controlling the deposition time, such as single NWs, Y-shaped branches, and interconnected NW or MW networks.[62]

2.4 2D Metal Halide Perovskite Nano/Microstructures

2.4.1 Perovskite nano/microplates

The unique and excellent properties of 2D structured perovskite such as NSs, NPs, and microdisks (MDs) make them promising for potential optoelectronic devices.[77] Sichert et al.[61] synthesized $MAPbBr_3$ NPs and investigated the quantum size effect of NPs via the solution method. They found that the thickness of $MAPbBr_3$ NPs was reduced with the increase of the content of OA [Figs. 5(a) and 5(b)]. Correspondingly, the PL emission was tuned from the green to violet region [Fig. 5(c)].[61] Qin et al. prepared $MAPbI_3$ NPs via a two-step solution method. First, PbI_2/DMF solvent was spin-coated onto a substrate to form PbI_2 thin films. Then, the formed PbI_2 thin film was immersed into MAI solution, in which $MAPbI_3$ single NCs were formed.[81]

$CsPbBr_3$ NPs were prepared by Bekenstein et al.[37] through a hot-injection method. They demonstrated that the reaction temperature is critical for the shape and thickness of $CsPbBr_3$ NPs. As the temperature decreased from 150°C to 130°C, the shape of $CsPbBr_3$ NCs evolved from nanocubes to NPs. Correspondingly, the PL emission was shifted from 512 to 405 nm [Figs. 5(d) and 5(e)].[37] When the temperature decreased to 90°C and 100°C, the thin $CsPbBr_3$ NPs were obtained with lengths of about 200 to 300 nm [Fig. 5(d)].[37] Except for the reaction temperature, surface ligands also affect the formation of $CsPbX_3$ NPs, which was demonstrated by Pan et al. in 2016. During the growth of NPs, $CsPbX_3$ NPs were obtained at a relatively lower reaction temperature (120°C to 140°C). They obtained thinner $CsPbX_3$ NPs with shorter chain amines.[82] In addition, the reaction time was also found to be critical for the formation of perovskite NPs.[78,79] By adding the $PbBr_2$ concentration and increasing the reaction time above 1 h (135°C), a $CsPb_2Br_5$ microplate (MP) with a micrometer order size and regular end faces could be obtained [Fig. 5(f)].[78] In 2018, Li et al. demonstrated that 2D $CsPbX_3$ NPs and NSs can be obtained by varying the reaction time [Fig. 5(g)]. The thickness can be controlled in the range of 3 to 6 nm and the width in the range of 0.1 to 1 μm.[79] Huang et al. reported a method for spontaneous crystallization of perovskite NCs in nonpolar organic solvent by mixing precursor ligand complexes without any heat treatment. By varying the ratio of monovalent to Pb^{2+} cation–ligand complexes, the shape of the NCs can be controlled from 3D nanocubes to 2D nanoplatelets.[83]

Similar to the NWs, perovskite NPs can also be formed by the vapor synthesis method. Xiong and coworkers[80] reported the CVD growth of $MAPbI_3$ NPs. These NPs exhibited triangular or hexagonal platelet shapes, with thickness of 10 to 300 nm and lateral dimensions of 5 to 30 μm [Figs. 5(h) and 5(i)]. PbX_2 platelets were first grown on mica via van der Waals epitaxy and then converted to $MAPbX_3$ NPs with the existence of MAX. In

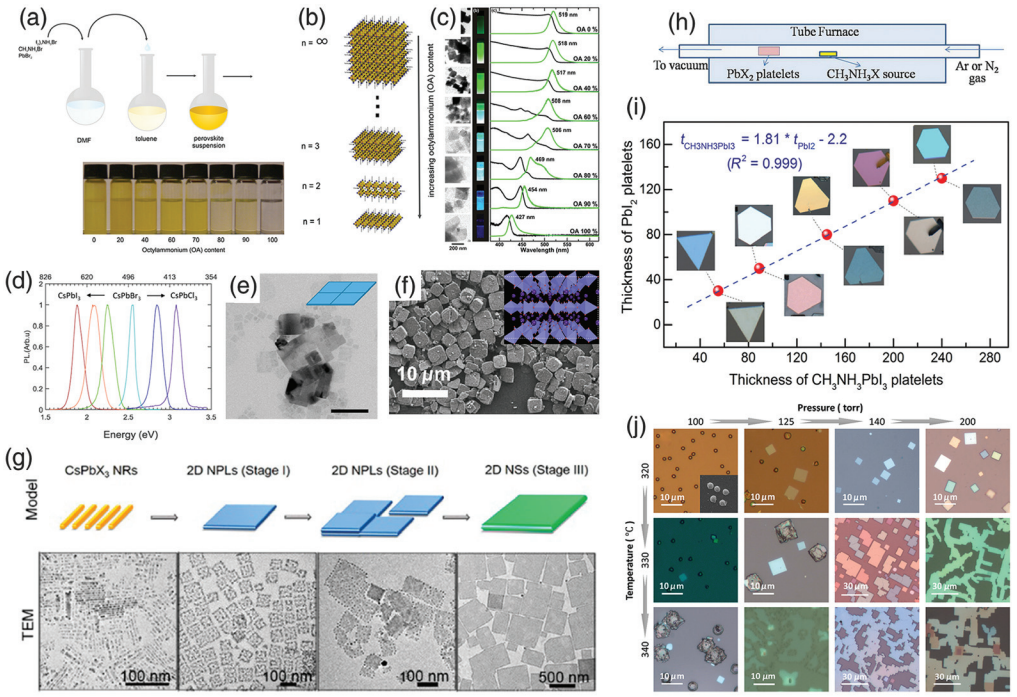

Fig. 5 (a) Schematic of the synthesis of $MAPbBr_3$ NPs. Figures reproduced from Ref. 61. (b) Quantum size effect in $MAPbBr_3$ NPs. Figures reproduced from Ref. 61. (c) Bandgap tuning in $MAPbBr_3$ NPs and micro/NRs via size or compositional control. Figures reproduced from Ref. 61. (d) PL spectra of the halide–anion exchanged $CsPbX_3$ NPs. Figures reproduced from Ref. 37. (e) 2D $CsPbBr_3$ NSs. Figures reproduced from Ref. 37. (f) SEM images of $CsPb_2Br_5$ MP. Figures reproduced from Ref. 78. (g) Top: Schematic of the growth of 2D $CsPbX_3$ NPs and NSs from $CsPbX_3$ NRs. Bottom: TEM images of $CsPbBr_3$ NCs for different times. Figures reproduced from Ref. 79. (h) Schematic of the fabrication of $MAPbI_3$ NCs using a vapor-transport system. Figures reproduced from Ref. 80. (i) Thickness of PbI_2 platelets before and after being converted to $MAPbI_3$. Figures reproduced from Ref. 80. (j) Optical images of as-grown $MAPbI_3$ NCs with different temperature and pressure. Figures reproduced from Ref. 64.

2016, Bao and coworkers developed a combined method containing a solution process and a vapor-phase conversion process to prepare $MAPbI_3$ NSs. First, PbI_2 flakes were dropped on a silica substrate and then heated. In this process, the temperature plays a crucial role in the nucleation and growth of 2D PbI_2 NSs, since the amount of nucleation sites is controlled by temperature. Subsequently, $MAPbI_3$ NSs were formed after the conversion reaction with MAI.[84] During the vapor-phase growth, the growth pressure and temperature both could affect the formation of perovskite NCs. Liu et al.[64] fabricated 2D $MAPbBr_3$ platelets (001) via the CVD method. As shown in Fig. 5(j), the square-shaped platelets could not form, as the growth pressure and temperature were low. By increasing the pressure, 2D platelets and 3D spheres could be observed. The average thickness of $MAPbBr_3$ platelets increased from 29 to 73 nm, and the lateral size increased from 6 to 10 μm with the pressure increasing from 140 to 200 Torr.[64]

As for all-inorganic 2D perovskite NCs, Zeng and coworkers[85] synthesized ultrathin $CsPbBr_3$ NPs (thickness ~148.8 nm) on a mica substrate by van der Waals epitaxy through heating the $PbBr_2$ and CsBr mixture. Zheng et al.[86] synthesized 2D $CsPbI_3$ perovskite NSs with high quality, controllable morphology, and ultrathin thickness (~6.0 nm) via a space-confined vapor-phase epitaxial growth. In 2020, Yang and coworkers developed a facile method to pattern $CsPbX_3$ plate arrays with crystal size (200 nm to 1 μm) and spacing (2 to 20 μm). These plate arrays were confined by prepatterned hydrophobic/hydrophilic surfaces.[65] The method can evade the restriction of lattice matching between perovskite and substrates, enabling a large-area growth of 2D perovskite NCs with excellent crystalline quality.[85]

2.4.2 Metasurface

A metasurface is a type of 2D optical element composed of units with subwavelength scale size, producing resonant coupling between electric and magnetic components of the incident electromagnetic fields.[87–91] Several functionalities were demonstrated on all-dielectric metasurfaces, such as optical encoding, optical wavefront molding, polarization beam splitter, and enhanced PL.[92–94] Perovskite-based metasurfaces demonstrated potential for nonlinear absorption and optical encoding.[95] Metasurfce structures can be realized by nanopatterning thin film. Many conventional nanofabrication techniques have been used for the fabrication of perovskite metasurfaces, such as nanoimprinting, electron beam lithography (EBL), focused ion beam milling (FIB), and inductively coupled plasma etching (ICP).[90,94,96–98]

Gholipour et al.[97] first used the FIB technique to fabricate $MAPbI_3$ metasurfaces (thickness ~200 nm), which consisted of nanogratings and nanoslit metamolecules. Moreover, they demonstrated that the emission and quality factor of the

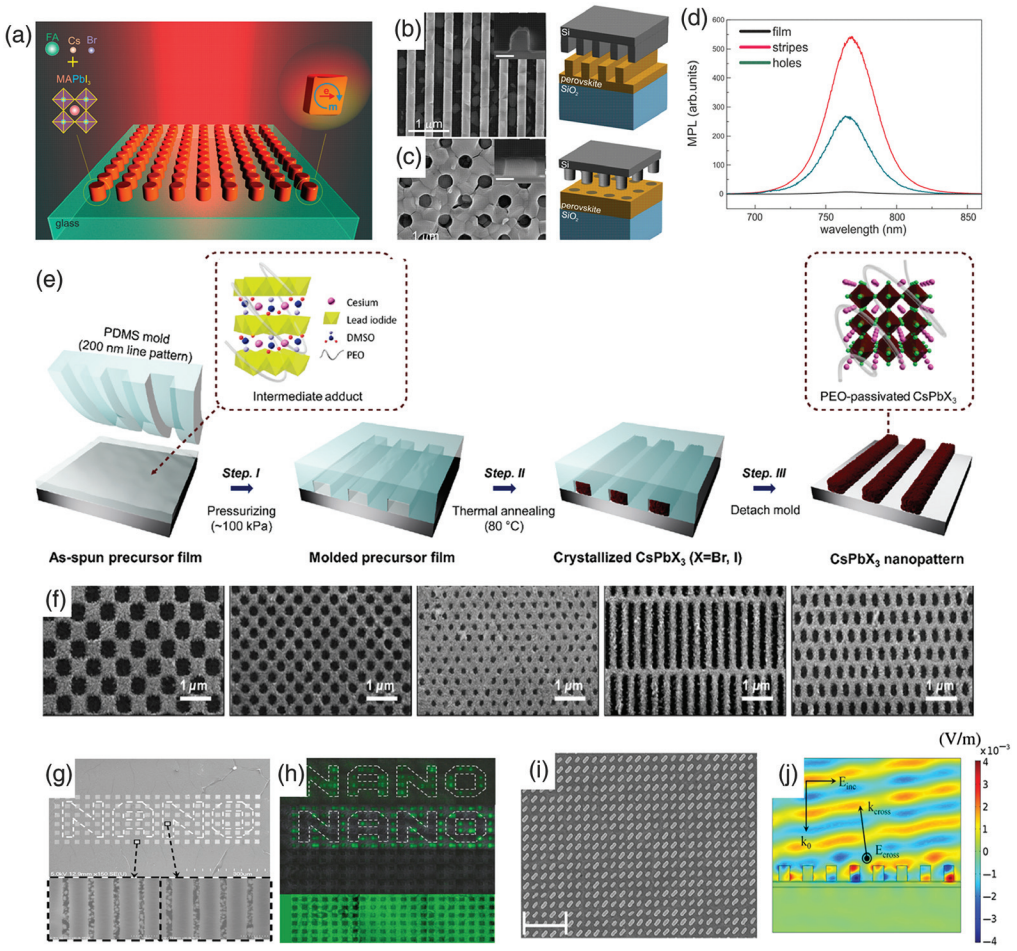

Fig. 6 (a) Perovskite metasurfaces with enhanced emission. Figures reproduced from Ref. 98. SEM images of perovskite with (b) nanostripe and (c) nanohole structures. Figures reproduced from Ref. 98. (d) Enhanced PL spectra from perovskite metasurfaces with different structures. Figures reproduced from Ref. 98. (e) Schematics of the polymer-assisted nanoimprinting process for perovskite nanopatterns. Figures reproduced from Ref. 94. (f) SEM images of various perovskite nanopatterns. Figures reproduced from Ref. 94. (g) SEM images of $MAPbBr_3$ metasurface for nonlinear imaging. Figures reproduced from Ref. 90. (h) The nonlinear PL and linear PL images of $MAPbBr_3$ metasurfaces. Figures reproduced from Ref. 90. (i) SEM image of $MAPbBr_3$ metasurface. Figures reproduced from Ref. 96. (j) The field distributions of $MAPbBr_3$ perovskite metasurface. Figures reproduced from Ref. 96.

reflection resonances can be tuned by varying the grating period.[97] Makarov et al.[98] developed nanoimprinting technology for patterning $Cs_\alpha FA_\beta MA_\gamma Pb(I_x Br_y)_3$ metasurfaces, enabling them to enhance their linear and nonlinear PL [Figs. 6(a)–6(d)]. After the spin-coating of the perovskite film with thickness of ∼200 nm, nanoimprinting with nanopillar and nanostripe molds was performed on perovskite thin film to form metasurfaces. They demonstrated that these metasurfaces can enhance linear PL eight times and nonlinear PL 70 times.[98] Jeong et al.[94] presented a polymer-assisted nanoimprinting method for fabricating large-area $CsPbX_3$ nanopatterns. As shown in Fig. 6(e), during their nanoimprinting process, a precursor solution was spin-coated on a substrate initially, and then the nanoimprinting mold was pressed on the precursor film with thermal treatment subsequently. Thus, $CsPbX_3$ was crystallized within the confines of molds [Fig. 6(f)]. This method could be easily extended to large-area perovskite patterns on different substrates.[94] In addition, Fan et al.[90] used the EBL flowed ICP technique to prepare near-infrared $MAPbBr_3$ perovskite metasurfaces [Fig. 6(g)]. Based on these metasurfaces, many types of nonlinear processes and enhanced PL could be observed [Fig. 6(h)].[90] The authors presented the application of perovskite metasurfaces on optical encryption.[90] The perovskite metasurface also can be used in optical phase control, which was confirmed by Zhang et al. in 2019. They also used the EBL flowed ICP technique to prepare $MAPbX_3$ cut-wire metasurfaces on metal substrates [Figs. 6(i) and 6(j)].[96] They found that these $MAPbX_3$ metasurfaces can generate a full phase control from 0 to 2π and high-efficiency and broadband polarization. Finally, they proved the potential application in holographic images based on the unique property of perovskite metasurfaces.[96]

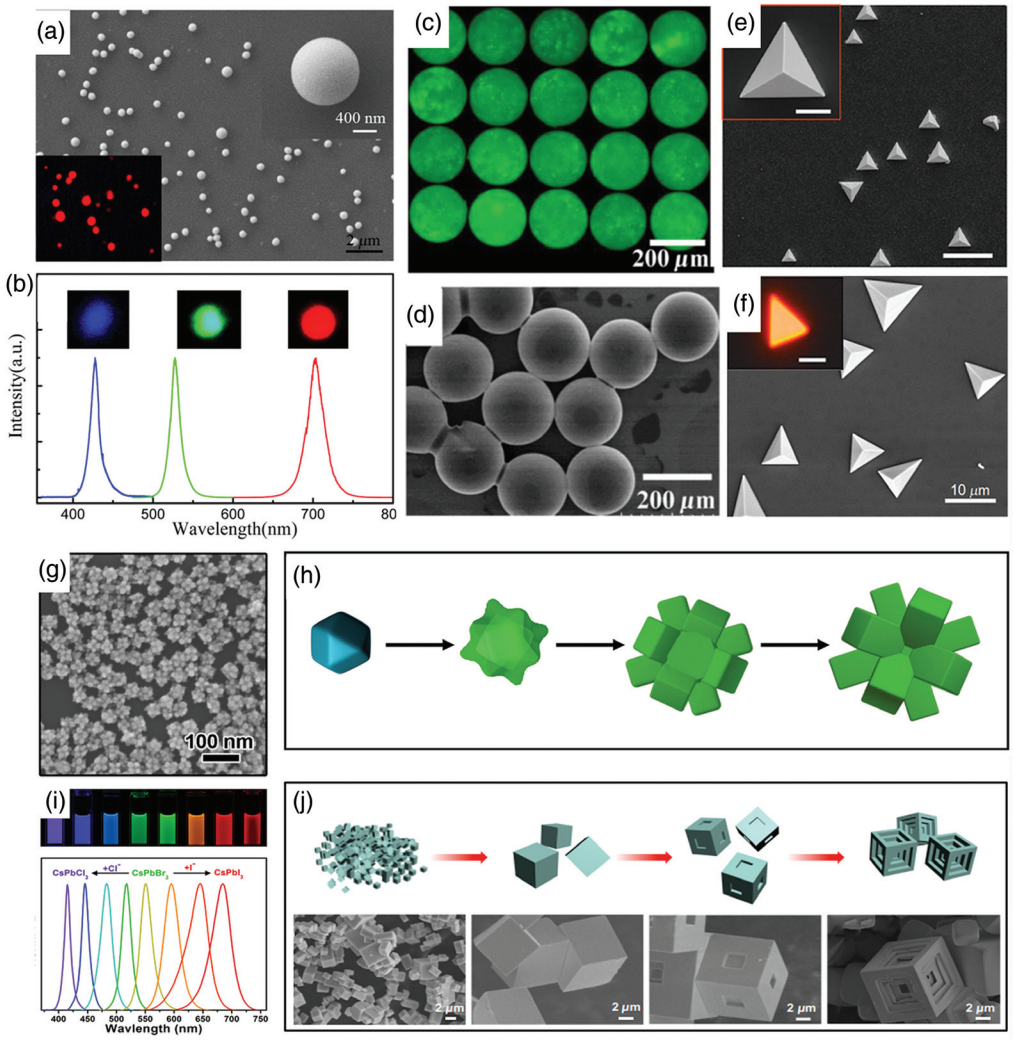

Fig. 7 (a) SEM image of the $CsPbI_3$ MSs. Figures reproduced from Ref. 100. (b) PL spectra of $CsPbCl_3$, $CsPbBr_3$, and $CsPbI_3$ MSs. Figures reproduced from Ref. 100. (c) Monodispersed $CsPbBr_3$ spheres under the excitation of UV light. Figures reproduced from Ref. 101. (d) SEM image of the monodispersed $CsPbBr_3$ spheres. Figures reproduced from Ref. 101. (e) SEM image of the $MAPbBr_3$ triangular pyramids. Figures reproduced from Ref. 102. (f) SEM image of the $CsPbI_3$ triangular pyramids on a Si/SiO_2 substrate. Figures reproduced from Ref. 103. (g) SEM image and (h) schematic of the formation of $CsPbX_3$ nanoflowers. Figures reproduced from Ref. 104. (i) Photograph (upper) and PL emission spectra (bottom) of $CsPbX_3$ nanoflowers. Figures reproduced from Ref. 104. (j) Crystal growth of $MAPbBr_3$ cuboids (top) and SEM images of $MAPbBr_3$ perovskite under different reaction time (bottom). Figures reproduced from Ref. 105.

2.5 3D Metal Halide Perovskite Nano/Microstructures

Besides 1D and 2D structured-perovskite, perovskite-based 3D structures have also been investigated. In 2017, a two-step method for the fabrication of $CsPbX_3$ microcubes with sub-wavelength size was developed by Hu et al.[99] These $CsPbX_3$ microcubes had a regular cube shape and smooth end faces, displaying tunable emission and excellent structure stability for several months under ambient conditions. In the same year, Zhang and coworkers used the CVD method on the prepared $CsPbX_3$ MSs with controlled diameter of ~1 μm and tunable PL ranging from 425 to 715 nm [Figs. 7(a) and 7(b)].[100] Wei et al.[101] developed an automated microreactor system to fabricate an inorganic perovskite NCs sphere by UV photoinitiated polymerization in flow-focusing microfluidics [Figs. 7(c) and 7(d)]. These obtained $CsPbBr_3$ spheres had a large diameter around 100 μm, and the diameter could be influenced by flow rates.[101] Mi et al.[102] used the CVD method to fabricate high-quality single $MAPbBr_3$ crystals with a cube-corner pyramids shape and lateral dimension in the range of 2 to 10 μm on mica substrates [Fig. 7(e)]. Then, Yang et al.[103] also used the CVD method to fabricate $CsPbI_3$ triangular pyramids with a spontaneous emission of ~719 nm at room temperature on a Si/SiO_2 substrate [Fig. 7(f)].

Except for the regular morphologies, complex perovskite structures have also been investigated. Chen et al.[104] used a seed-mediated solvothermal method to fabricate monodisperse $CsPbX_3$ NCs with nanoflower morphology [in Figs. 7(g)–7(i)].

Figure 7(h) shows the growth process of $CsPbBr_3$ nanoflowers, which is formed by the structure transformation from Cs_4PbBr_6 to $CsPbBr_3$. It is obtained that $CsPbX_3$ dodecapods contained 12 well-defined branches, with a PLQY of about ~50%. Moreover, the PL emission could be tuned from 415 to 685 nm. They prepared a white LED device based on using $CsPbBr_3$ nanoflowers, exhibiting the 135% National Television System Committee (NTSC) standard.[104] In 2019, Li et al. fabricated single crystal microcuboid-$MAPbBr_3$ and multistep-$MAPbBr_3$ NCs via the solvothermal method at 120°C. In this process, microcuboid-$MAPbBr_3$ was formed initially, and then the center of the surface was etched after long-time reaction, inducing the formation of multisteps. By adjusting the reaction temperature and time, the morphology and size of microcuboid-$MAPbBr_3$ [Fig. 7(j)] could be adjustable, with performing potential in perovskite nanolaser and other optoelectronic devices.[105]

3 Perovskite-Based Laser

3.1 Nonlinear Optical Properties

Nonlinear optics describes the nonlinear state of the interaction between light and matter.[106–111] The researches on optical nonlinear materials are fundamental to nonlinear optics devices such as optical storage, optical switches, optical amplifiers, and lasers.[112–114] Due to the multiformity of physical and chemical properties, halide perovskites have been demonstrated as promising materials as nonlinear optics materials, which are related to the component and crystal structure of perovskite NCs.[106]

In 2015, Sargent and coworkers investigated two-photon absorption in $MAPbBr_3$ single crystals, under ultrashort pulses 800 nm excitation [Figs. 8(a)–8(d)]. They observed two-photon PL around ~572 nm with an absorption coefficient of $8.6 \pm 0.5\ cm\ GW^{-1}$ at 800 nm.[117] Later, Heiko et al. performed temperature-dependent PL measurements on $MAPbBr_3$ single crystals under 810 nm excitation. They observed obvious wavelength shifts of PLs with variable temperatures, which was attributed to discrete transitions between several stable crystalline phases of $MAPbBr_3$ single crystals.[115] In 2016, Kalanoor et al. studied the nonlinear optical responses of $MAPbI_3$ films by the Z-scan technique, under nanosecond and femtosecond pulsed lasers. The nonlinear refractive index under femtosecond excitation was $\sim 69 \times 10^{-12}$ and $\sim 34.4 \times 10^{-9}\ cm^2/W$ for resonant nanosecond excitation, which was equivalent to conventional semiconductors.[118] The Z-scan study of $MAPbX_3$ (X = Cl, Br, I) perovskite film under the 800 nm, 40 fs pulse indicated that $MAPbI_3$ films have a relatively large nonlinear optical coefficient compared with the $MAPbCl_3$ and $MAPbBr_3$ films.[119] In the case of inorganic perovskites, Sun and coworkers discovered nonlinear optical properties of $CsPbX_3$ NCs for the first time [Figs. 8(e)–8(g)]. They observed strong two-photon absorption from 9-nm-sized $CsPbBr_3$ NCs, with a large absorption cross-section of $\sim 1.2 \times 10^5$ GM.[116] The nonlinear optical properties of $CsPbX_3$ perovskite are highly correlated with their morphology. Jiang and coworkers[120] investigated nonlinear optical properties of $CsPbBr_3$ NSs with a dependence on their thickness. When the thickness of $CsPbBr_3$ NS was adjusted from ~104.6 to ~195.4 nm, PL intensity increased nearly three times. They demonstrated that the two-photon absorption coefficient is inversely proportional to the thickness of $CsPbBr_3$ NSs.[120] Krishnakanth et al. investigated nonlinear optical properties from nanocubes and NRs by Z-scan technology, under femtosecond 600, 700, and 800 nm lasers. They obtained large two-photon absorption cross sections of $\sim 10^5$ GM and strong nonlinear optical susceptibility of $\sim 10^{-10}$ esu in these films.[121]

The laser is a process of amplifying optical signals and generating high-intensity coherent light through stimulated radiation and is usually composed of three parts: energy pumping

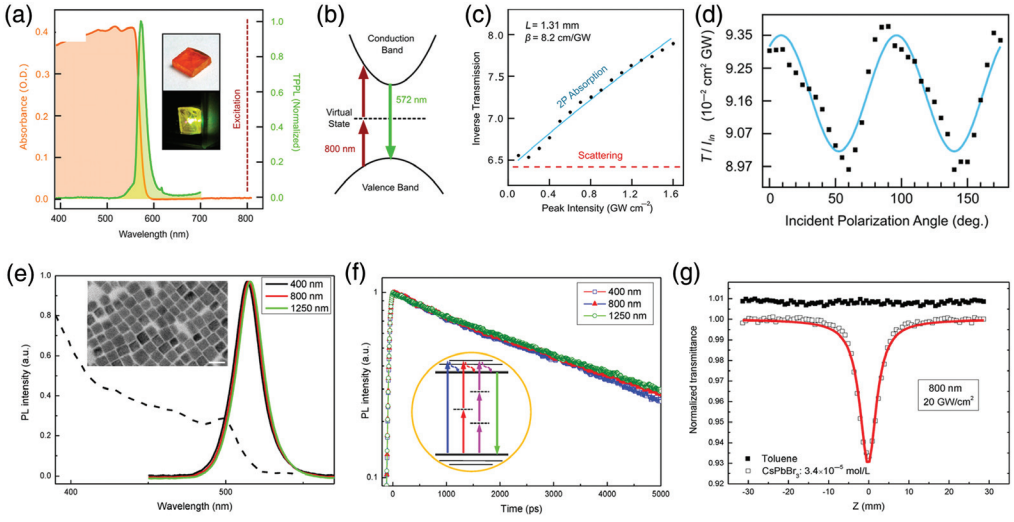

Fig. 8 (a) Absorption spectrum and normalized two-photon PL spectra of single $MAPbBr_3$ NCs. Figures reproduced from Ref. 115. (b) Schematic of two-photon absorption at 800 nm in perovskite. Figures reproduced from Ref. 115. (c) Two-photon absorption coefficient. (d) Inverse transmission versus peak intensity for typical single $MAPbBr_3$ NCs. Figures reproduced from Ref. 115. (e)–(g) Nonlinear optics of $CsPbX_3$ NCs: (e) linear absorption spectrum and normalized PL spectra from $CsPbBr_3$ NCs, (f) PL decay of $CsPbBr_3$ NCs, and (g) Z-scan responses of the $CsPbBr_3$ NC solution and the pure solvent. Figures reproduced from Ref. 116.

source, gain medium, and optical resonator. The amplification of the laser can be quantified as the resonance ability of gain media.[122,123] For gain media, the optical gain of the semiconductor is similar to the optical absorption, which is suitable for perovskite.[124,125] At the same time, optical losses are generated in optical cavities, which mainly come from nonradiative recombination, phonon scattering, edge scattering, and field leakage in the interface of cavities.[126] Perovskite materials have ultralow density, inducing high optical gain and low optical losses for resonance in perovskite, enabling promising potential in perovskite lasers with low threshold. The optical gain of semiconductors can be calculated by the variable-stripe-length measurement, which is related to the dependence of the amplified luminescence on the length of the slit width of the excitation. Xing et al.[23,124] performed variable stripe length measurements on $MAPbI_3$ with a gain coefficient of ~250 cm^{-1}, which was close to that of conventional semiconductor materials. The obtained optical gain coefficients of $MAPbBr_3$ and $MAPbCl_3$ were ~300 and ~110 cm^{-1}, respectively.[127,128] Liu et al.[129] demonstrated that the optical gain coefficient of $CsPbBr_3$ nanocuboids can be calculated to be ~502 cm^{-1} under the 800 nm laser. Then, Zhao et al. reported efficient two-photon ASE from $CsPbBr_3$ single crystals with a millimeter size and an optical gain of 38 cm^{-1}.[130]

3.2 Perovskite QDs Laser

In the case of perovskite QDs without an external cavity, the amplification was generated from multiple scattering between QDs, enabling random fluctuations of lasing modes.[127] In 2015, Kovalenko and coworkers reported low-threshold ASE from colloidal $CsPbX_3$ NCs with an optical gain coefficient of ~450 cm^{-1} and threshold of ~5 $\mu J/cm^2$.[127] In Figs. 9(a)–9(c), the ASE from $CsPbX_3$ NCs could be tuned from 440 to 700 nm. Finally, they obtained random lasing from $CsPbX_3$ films without the resonant cavity and whispering gallery mode (WGM) lasing using a silica sphere as the resonant cavity [Fig. 9(c)].[127] Besides, coating perovskite QDs onto an external cavity, Zeng and coworkers developed another method to form resonant cavities for perovskite QDs. They obtained enhanced random lasing from strong scattering in the perovskite/SiO_2 composite with low threshold of ~40 $\mu J/cm^2$ [Figs. 9(d)–9(f)].[131] Similarly, Yang et al.[136] realized upconversion random lasing from $FAPbBr_3$/A-SiO_2 composites with a threshold of ~413.7 $\mu J/cm^2$. Liu et al.[137] obtained WGM and random lasing with a threshold of ~430 $\mu J/cm^2$ under 800 nm excitation by embedding $CsPbBr_3$ QDs into a single silica sphere. In addition, microcapillary tubes can also be used to build WGM cavities for perovskite QDs. In 2015, Zeng and coworkers observed lasing emission from $CsPbBr_3$ QDs by filling the $CsPbBr_3$ QDs into a capillary tube, which acted as a WGM cavity for perovskite QDs film around the inner wall.[138] Later, stable two-photon pumped WGM lasing was realized by coupling $CsPbBr_3$ and $FAPbBr_3$ perovskite QDs into microtubules with thresholds of ~0.8 and ~0.31 mJ/cm^2 [Figs. 9(g)–9(j)], respectively.[132,139]

Besides the realization of perovskite QDs lasing-based silica sphere and microcapillary tube, the well-designed distributed Bragg reflector (DBR) can also be used to achieve a vertical-cavity surface-emitting laser (VCSEL).[133–135] In 2017, Zeng and coworkers first fabricated VCSELs with a sandwiched structure of DBR/$CsPbBr_3$ QDs/DBR, which exhibited a low threshold ~9 $\mu J/cm^2$ directional output and favorable stability [Fig. 9(k)].[133] The lasing emission of $CsPbX_3$-based VCSELs can be tuned in the visible light range.[133] In the same year, Huang et al.[134] fabricated $CsPbBr_3$ QDs VECSLs with ultralow threshold of ~0.39 $\mu J/cm^2$ [Fig. 9(l)]. Organic hybrid perovskites-based VCSELs have also been performed. Chen and Nurmikko[135] developed $FAPbBr_3$-based VCSELs by embedding $FAPbBr_3$ solid thin films in two DBRs [Fig. 9(m)] with a threshold of ~18.3 $\mu J/cm^2$ under subnanosecond pulse excitations. They also demonstrated that the VCSEL device fabrication process can be applicable to flexile substrates, as shown in Fig. 9(m), which extended further practical applications for perovskite-based laser devices.[135] Most recently, Li et al.[140] fabricated a two-photon-pumped $MAPbBr_3$ VCSEL by intergrading $MAPbBr_3$ with DBR and Ag mirrors with a threshold of ~421 $\mu J/cm^2$, a Q factor of ~1286, and a small divergence of ~0.5 deg.

3.3 Perovskite Nanowire/Nanorod Laser

Owing to the difference between the refractive index of perovskite material and air, the reflection can occur at the output interface easily, acting as optical reflector.[141,142] Hence, different from QDs, single perovskite crystals structures such as rods, wires, plates, cubes, and spheres can act as Fabry–Pérot (F-P) or WGM cavities by themselves, since the light can be confined in the resonant cavity with regular morphology and smooth end faces.[125] For the 1D NWs structure, light will propagate along 1D and form resonance between two end-facets.[143] Hence, perovskite NWs and NRs have been confirmed as potential structures in optoelectronic devices and nanoscale-integrated photonics due to their unique optical properties, such as highly coherent output and efficient waveguide effect.[143]

Zhu et al.[144] demonstrated perovskite NW lasers using high-quality $MAPbX_3$ NWs, which had a regular shape with rectangular cross section [Fig. 10(a)]. Tunable F-P lasing could be observed from single $MAPbX_3$ NWs with low threshold of ~0.22 $\mu J/cm^2$ and Q factor of ~3600 at room temperature [Figs. 10(b) and 10(c)]. In the same year, Xing et al.[49] realized F-P lasing from $MAPbI_3$ NWs with rectangular morphology and length of ~20 μm. The obtained NW laser exhibited low threshold of ~11 $\mu J/cm^2$ and Q factor of ~405, and the lasing wavelength could be tuned in the range of 551 to 777 nm.[49] In case of lasing from all-inorganic perovskite NWs, Yang and coworkers realized F-P lasing from $CsPbBr_3$ NWs with a threshold of ~5 $\mu J/cm^2$ and a Q factor of ~1009.[55] Fu et al. realized wavelength widely tunable F-P lasing from $CsPbX_3$ NWs. The lasing wavelength could be tuned in the visible spectral region from 420 to 710 nm [Figs. 10(e)–10(g)].[145] In 2017, lasing emission from triangular $CsPbX_3$ micro/NRs with an ultrasmooth surface by the vapor-phase approach was reported. The obtained lasing could be tuned in the range from 428 to 628 nm, with low threshold of ~14.1 $\mu J/cm^2$ and high Q factor of ~3500.[75] Efficient multiphoton pumped lasing in a wide excitation wavelength range (700 to 1400 nm) was realized.[147] Most of the single perovskite NWs mainly exhibited single-band lasing emission. In 2020, Tang et al. fabricated a single $CsPbCl_{3-3x}Br_{3x}$ alloy NW via a solid–solid anion-diffusion process. They realized continuous F-P lasing in single as-prepared NWs, which could be tuned from 480 to 525 nm [Figs. 10(i) and 10(j)].[146]

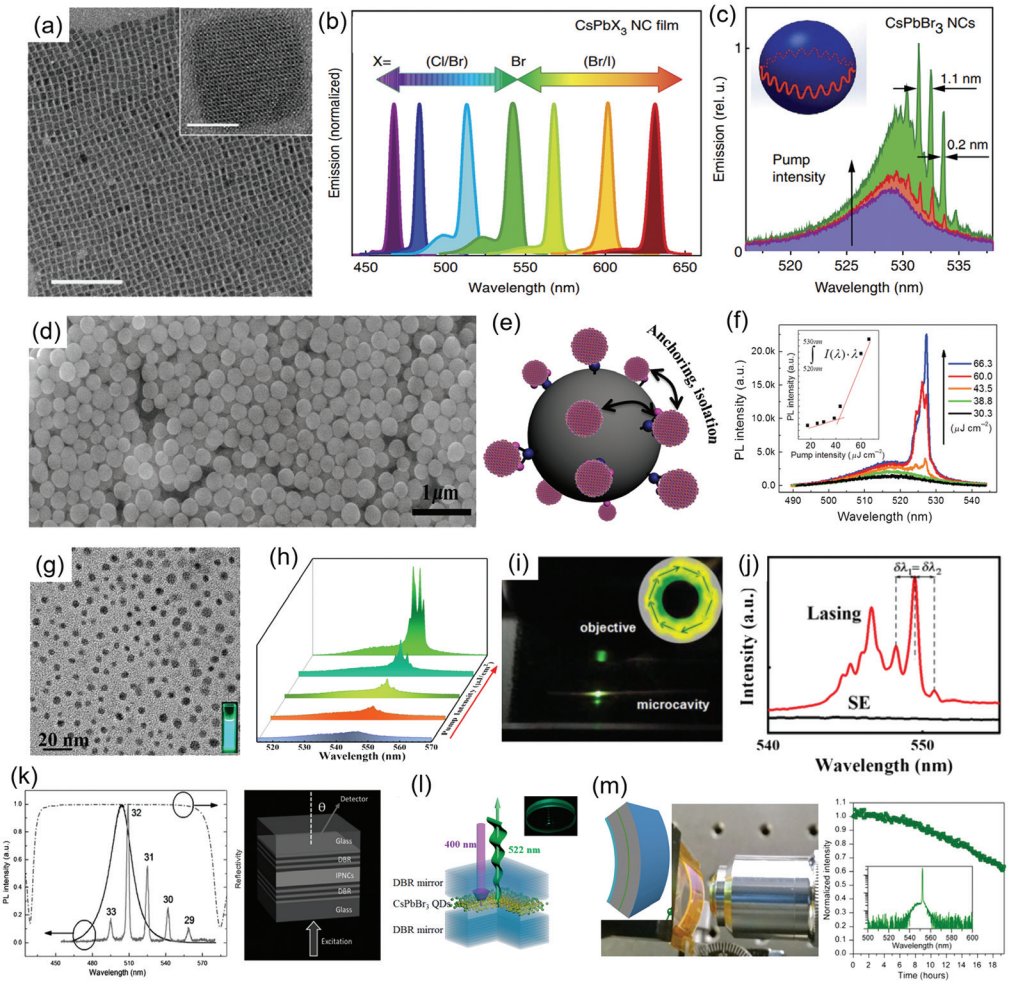

Fig. 9 (a) TEM images of $CsPbBr_3$ QDs. Figures reproduced from Ref. 127. (b) Spectral tunability of ASE of $CsPbX_3$ via compositional modulation. Figures reproduced from Ref. 127. (c) Evolution from PL to lasing in an MS resonator with increasing pump intensity. Figures reproduced from Ref. 127. (d) SEM image and (e) isolation effect of $CsPbBr_3$ QDs/A-SiO_2 composites. Figures reproduced from Ref. 131. (f) PL spectra from $CsPbBr_3$ QDs/A-SiO_2 composite with increasing pump intensity. Figures reproduced from Ref. 131. (g) TEM image of $FAPbBr_3$ QDs. (h) Two-photon PL spectra from $FAPbBr_3$ NCs in a microcapillary tube. (i) Optical image and (j) lasing emission spectra from $FAPbBr_3$ NCs in a microcapillary tube. Figures reproduced from Ref. 132. (k) Left: PL spectra from $CsPbBr_3$ film within/without microcavity. Right: Schematic of the $CsPbBr_3$ VCSEL. Figures reproduced from Ref. 133. (l) Schematic of the $CsPbBr_3$ VCSEL. Figures reproduced from Ref. 134. (m) Photograph and PL stability of flexible $FAPbBr_3$ VCSEL. Figures reproduced from Ref. 135.

3.4 Perovskite Nano/Microplate Laser

Different from the F-P cavity formed by NWs/NRs, the perovskite 2D structure such as NPs will result in the WGM optical resonant cavity, which has a higher Q factor than the F-P cavity. In 2014, Zhang et al. first realized WGM lasing from $MAPbI_3$ NPs with well-defined hexagonal and triangular shapes under femtosecond-pulsed laser excitation. The lasing wavelength was located at ~780 nm with a threshold of ~37 $\mu J/cm^2$ [Figs. 11(a)–11(d)].[80] Liao et al.[150] obtained single-mode WGM lasing from single $MAPbBr_3$ MDs peaked at ~557.5 nm with a threshold of ~3.6 $\mu J/cm^2$ and Q factor of ~430. Liu et al. realized WGM lasing from $MAPbI_3$ MP arrays with low threshold of ~11 $\mu J/cm^2$ and Q factor of ~1210.[151] Moreover, they observed single mode lasing by shortening the size of MPs.[151] Qi et al.[152] demonstrated that the threshold of the MPs laser decreases linearly depending on the later size, and the cavity mode density increases with the size. In 2019, WGM lasing from a triangular $MAPbI_3$ perovskite NP with a lateral length of 27 μm and thickness of 80 nm was realized at room temperature. The threshold of the WGM laser was ~18.7 $\mu J/cm^2$ and Q factor was ~2600 [Figs. 11(e)–11(i)].[148]

As for the 2D all-inorganic perovskite-based laser, Zhang et al.[149] obtained WGM excitonic lasing from single-crystalline $CsPbX_3$ NPs with micron-size length and subwavelength thickness [Figs. 11(j)–11(m)]. Multicolor lasing from 410 to

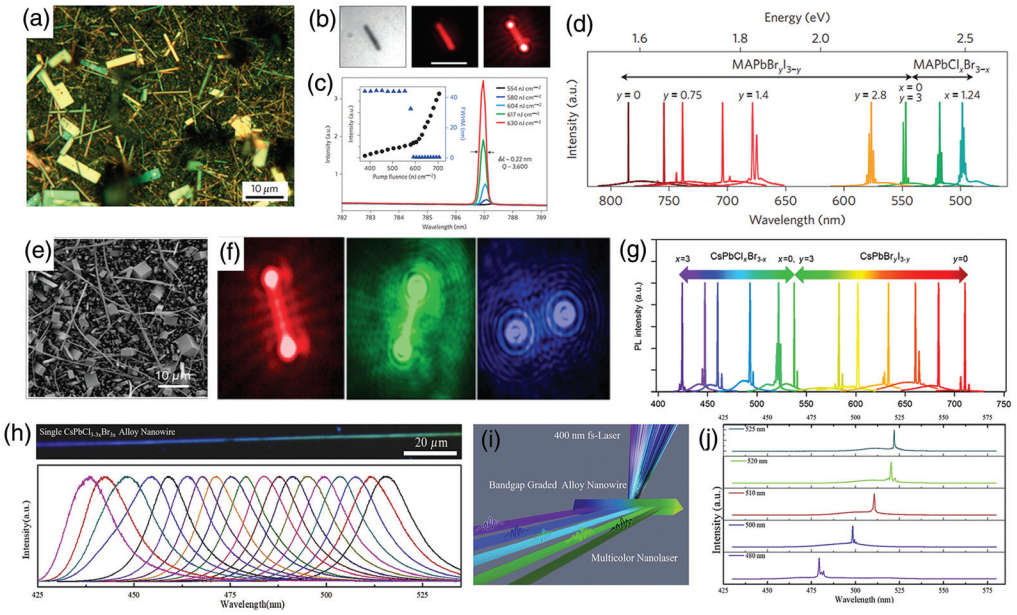

Fig. 10 (a) SEM of $MAPbI_3$ nanostructures. Figures reproduced from Ref. 144. (b) Optical image of single $MAPbI_3$ NW. Figures reproduced from Ref. 144. (c) PL spectra of $MAPbI_3$ NW around the lasing threshold. Figures reproduced from Ref. 144. (d) Broad tunable lasing from single-crystal $MAPbX_3$ NW. Figures reproduced from Ref. 144. (e) SEM image of $CsPbBr_3$ nanostructures. Figures reproduced from Ref. 145. (f) Fluorescence images of red/green/blue $CsPbX_3$ NWs above lasing threshold. Figures reproduced from Ref. 145. (g) Broad tunable lasing from single-crystal $CsPbX_3$ NWs. Figures reproduced from Ref. 145. (h) The photograph and PL spectra of a single $CsPbCl_{3-3x}Br_{3x}$ NW. Figures reproduced from Ref. 146. (i) The schematic of optically pumping lasing from a single $CsPbCl_{3-3x}Br_{3x}$ NW. Figures reproduced from Ref. 146. (j) Typical lasing spectra from a single $CsPbCl_{3-3x}Br_{3x}$ NW. Figures reproduced from Ref. 146.

700 nm was realized in these NPs at room temperature [Fig. 11(l)]. The lasing threshold of the $CsPbX_3$ NP was as low as ~2.0 $\mu J/cm^2$, and the linewidth of the WGM modes was ~0.14 to 0.15 nm [Fig. 11(m)].[149] Zheng et al.[86] demonstrated that $CsPbI_3$ perovskite NSs possess WGM lasing under both one- and two-photon pumps with low-threshold-pumped excitation [Figs. 11(n)–11(q)]. The thresholds of lasing were ~0.30 and ~2.6 mJ/cm^2 under one- (470 nm) and two-photon (1200 nm) excitation, and the Q factors were ~1489 and ~1179, respectively, which is three times higher than the reported values of organic–inorganic lead halide perovskite NS. Most recently, Liu et al.[153] realized two lasing modes (F-P and WGM) in the all-inorganic perovskite $CsPb_2Br_5$ MPs with subwavelength thickness and uniform square shape under two-photon pump. Remarkably, low-threshold F-P multimode lasing with Q factor of ~3551 and single-mode WGM lasing with Q factor of ~3374 from the same MP at room temperature have been achieved successfully.

3.5 Perovskite Laser with 3D Structure

A single perovskite spherical 3D structure has also usually been demonstrated as a WGM cavity. In comparison with other nano/microstructure resonant cavities, the coupling between the sphere cavity and substrate was relatively weak, which resulted in less optical losses. Zhang and coworkers realized single-mode lasing in $CsPbX_3$ MSs with regular sphere shape and submicron size at room temperature [Figs. 12(a)–12(d)].[100] The line width of WGM lasing was ~0.09 nm, the threshold was ~0.42 $\mu J/cm^2$, and Q factor was ~6100 [Fig. 12(c)]. In addition, the single-mode lasing can be tuned in the whole visible region through element modulation and size control of perovskite MSs [Fig. 12(d)].[100] Furthermore, they achieved two-photon single-mode lasing with linewidth of ~0.037 nm and Q factor of ~1.5×10^4 from a single $CsPbBr_3$ MS at room temperature, which are the best values obtained in perovskite-based micro/nanocavities until now.[154] Moreover, these perovskite MS lasers showed uniform lasing emission, which could be observed in the range from −30 deg to 30 deg.[154,155]

Another 3D structure generally used for perovskite lasing is the nano/microcube. Liu et al.[129] obtained F-P lasers from an individual $CsPbBr_3$ nanocuboid with subwavelength scale for the first time [Figs. 12(e)–12(h)]. They realized single-mode F-P lasing from a $CsPbBr_3$ nanocuboid with low thresholds of ~40.2 and ~374 $\mu J/cm^2$ and Q factors of ~2075 and ~1859 under one- and two-photon pumps, respectively.[129] The physical volume of the obtained laser is ~0.49 λ^3. Moreover, the pulse duration is only ~22 ps, which is consistent with the resulting fast decay of SE observed by fs transient absorption spectroscopy [Fig. 12(h)].[129] Cube-corner pyramid cavities could also act as microretroreflectors. In 2018, Mi et al. realized F-P lasing in cube-corner $MAPbBr_3$ pyramids at room temperature [Figs. 12(i)–12(m)].[102] Furthermore, the threshold of lasing could be reduced from ~92 to 26 $\mu J/cm^2$ by coating a thin layer of Ag film on a mica substrate [Figs. 12(l) and 12(m)].[102] Most recently, Yang et al.[103] also realized F-P lasing from a single

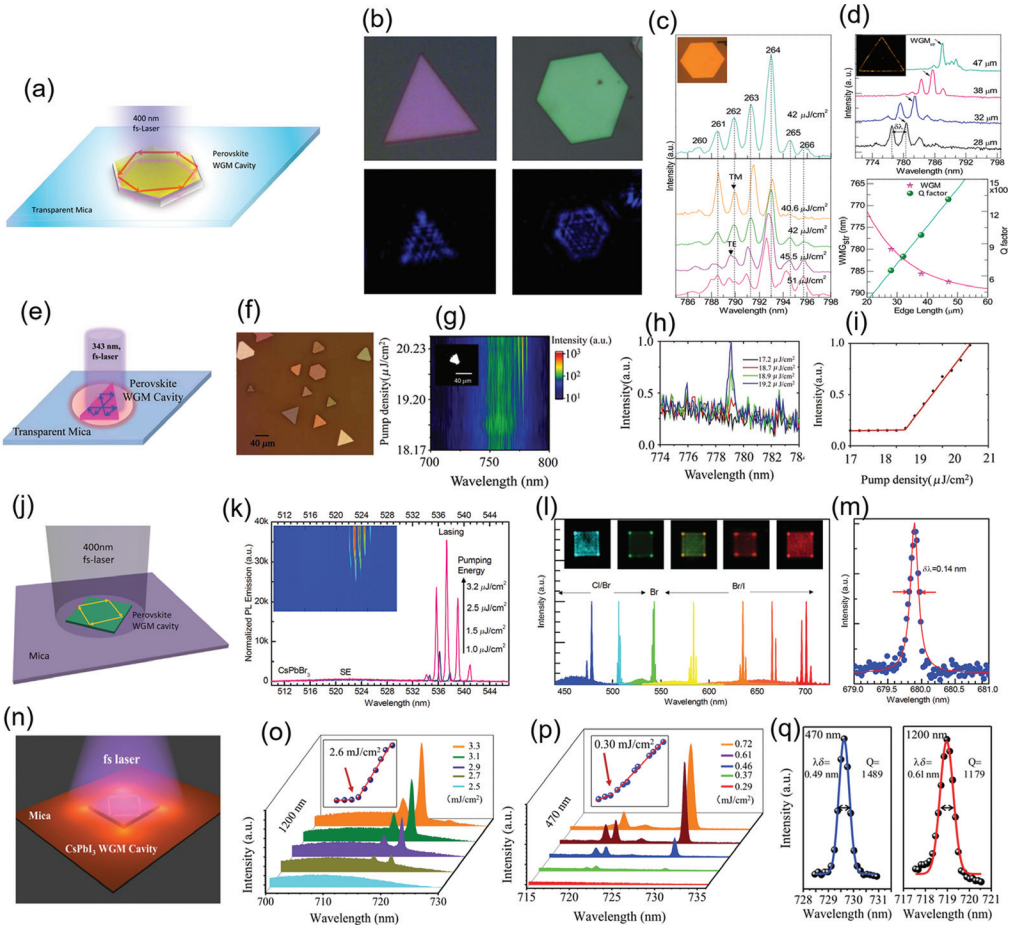

Fig. 11 (a) Schematic of an $MAPbX_3$ NP pumped by a pulsed laser. Figures reproduced from Ref. 80. (b) Optical image of $MAPbI_3$ NPs under white light and laser excitation. Figures reproduced from Ref. 80. (c) Lasing spectra of hexagonal $MAPbI_3$ NPs (upper) and the lasing mode evaluation with pumping fluence (bottom). Figures reproduced from Ref. 80. (d) Upper: Lasing spectra of triangular $MAPbI_3$ NPs with different edge length. Bottom: The wavelength of lasing modes and *Q*-factor as a function of the triangular cavity edge length. Figures reproduced from Ref. 80. (e) Schematic of triangular $MAPbI_3$ NPs pumped by a 343 nm laser. Figures reproduced from Ref. 148. (f) Optical image of triangular $MAPbI_3$ NPs. Figures reproduced from Ref. 148. (g) 2D plot of a triangular $MAPbI_3$ NP emission under different pump densities. Figures reproduced from Ref. 148. (h) The emission spectra from $MAPbI_3$ NPs around the lasing threshold. Figures reproduced from Ref. 148. (i) Output emission intensity as a function of pump densities. Figures reproduced from Ref. 148. (j) Schematic of a $CsPbX_3$ plate under a 400 nm laser. Figures reproduced from Ref. 149. (k) Emission spectra at different pump intensities. Figures reproduced from Ref. 149. (l) Tunable lasing spectra and images of individual $CsPbX_3$ perovskite NPs. Figures reproduced from Ref. 149. (m) Single-mode lasing of $CsPbBr_xI_{3-x}$. Figures reproduced from Ref. 149. (n) Schematic of a $CsPbI_3$ NS on mica substrate. Figures reproduced from Ref. 86. Excitation intensity-dependent emission spectra under (o) 470 nm and (p) 1200 nm excitation. Figures reproduced from Ref. 86. (q) Gaussian fitting of a lasing mode under 470 and 1200 nm laser. Figures reproduced from Ref. 86.

$CsPbI_3$ triangular pyramid with a microsize at low temperature. They demonstrated that the temperature-dependent lasing threshold can be reduced from ~53.15 to 21.56 $\mu J/cm^2$ with corresponding temperature from 223 to 148 K.[103]

3.6 Perovskite Nanolaser Array

In comparison with single perovskite lasers, laser arrays with high-density patterns and high-precision arrangements are more necessary for mass-produced, compact on-chip optoelectronic circuit integration. In 2016, Wang et al. fabricated $MAPbBr_3$ microwire arrays and realized high density perovskite lasers from these microwire arrays [Figs. 13(a) and 13(b)], in which all of the subunits generated the same lasing emission.[156] The minimum unit period was 800 nm, presenting an integration density of nanolasers as high as 1250 mm^{-1}. In 2017, Fu and coworkers prepared $MAPbBr_3$ NW arrays with the width from 460 to 2500 nm, height from 80 to 1000 nm, and length from

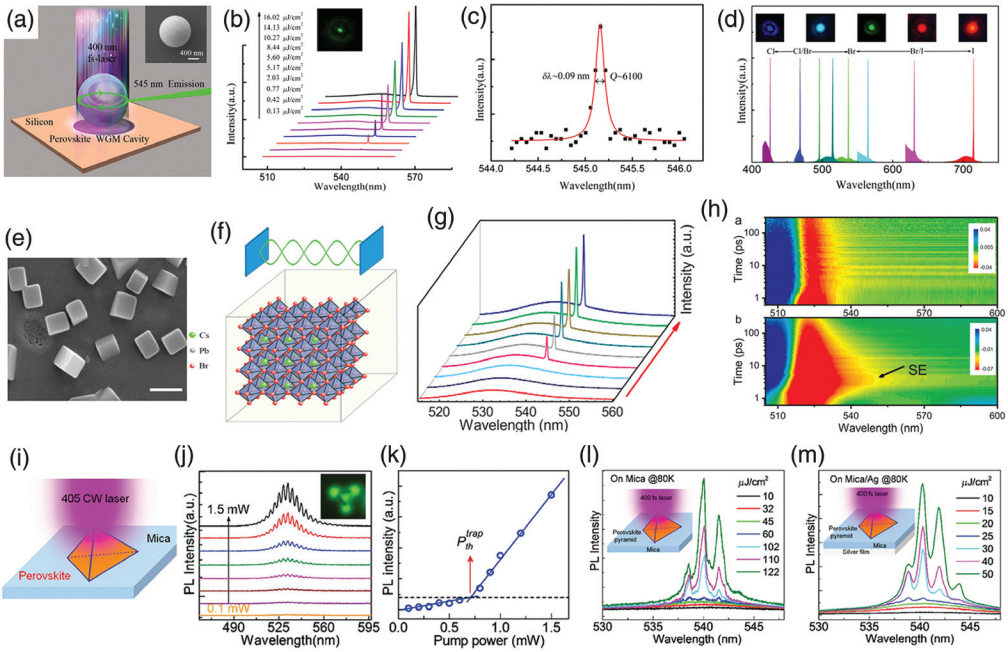

Fig. 12 (a) Schematic of a single $CsPbBr_3$ MS under 400 nm laser. Figures reproduced from Ref. 100. (b) Lasing PL spectra from a single $CsPbBr_3$ MS under different pump intensities. Figures reproduced from Ref. 100. (c) Lorentzian fitting of a lasing mode. Figures reproduced from Ref. 100. (d) Photograph and lasing emission of multicolor $CsPbX_3$ MS lasers. Figures reproduced from Ref. 100. (e) SEM image and (f) schematics of F-P cavity of $CsPbBr_3$ nanocuboids. Figures reproduced from Ref. 129. (g) Single-mode lasing spectra and (h) TA spectroscopic data of $CsPbBr_3$ nanocuboids under two-photon excitation. Figures reproduced from Ref. 129. (i) Schematic of a cube-corner $MAPbBr_3$ pyramid under 405 nm laser. Figures reproduced from Ref. 102. (j) PL spectra of a cube-corner $MAPbBr_3$ and (k) output intensity as a function of excitation power. Figures reproduced from Ref. 102. (l), (m) Multimode lasing spectra of a cube-corner pyramid of $MAPbBr_3$ on (l) mica and (m) mica/Ag. Figures reproduced from Ref. 102.

10 to 50 μm. These perovskite NW arrays were demonstrated as almost identical optical resonance cavities with a low threshold of ~10.2 $\mu J/cm^2$ [Figs. 13(c) and 13(d)].[157] In 2016, Liu et al. realized WGM lasing from patterned $MAPBI_3$ microplatelets arrays with a threshold of ~11 $\mu J/cm^2$ and Q factor up to ~1210. The wavelength tunability and single mode lasing could be selected by changing platelet sizes or breaking the symmetry of the designed laser pattern.[151] In the same year, Feng et al.[158] demonstrated that the $MAPbBr_3$ square MP array shows high-performance WGM lasing with tunable mode and low lasing threshold [Figs. 13(e) and 13(f)]. Single mode lasing was obtained from a 2.1-μm $MAPbBr_3$ square. Lin et al.[159] fabricated a large-area $CsPbX_3$ QDs array by a photolithographical approach, which could be used as efficient lasing structures and emitting pixel arrays [Figs. 13(g)–13(i)]. They realized WGM lasing from the QD arrays with high Q factor and demonstrated that this patterning technique can be used in large-area perovskite laser arrays with multicolor pixels [Fig. 13(g)].[159] Most recently, Wang et al.[160] fabricated large-area $MAPbX_3$ MD arrays via a screen-printing technique [Figs. 13(j)–13(m)]. They obtained tunable WGM lasing from these $MAPbX_3$ MD arrays with a threshold of ~21.3 $\mu J/cm^2$ and a Q factor of ~1570 successfully. Multicolor WGM lasing emission could be tuned from ~510 to 650 nm [Fig. 13(l)].[160] In 2020, Song and coworkers employed the topologically protected optical bounded states in the continuum (BICs) and demonstrated the ultrafast control of perovskite-based vortex microlasers at room temperature. They proved that vortex beam lasing based on perovskite metasurfaces could be switched to linearly polarized beam lasing with switching time of 1 to 1.5 ps. The energy consumption was several orders of magnitude lower than that of previously reported all-optical switching.[161]

3.7 Others

Surface-plasmon (SP) is an excited state with large enhancement of the electromagnetic field localized at the metal–dielectric interface, which provides confinement on the subwavelength scale, overcoming the diffraction limit of light.[162] In perovskite micro/nanolasers, SPs have been demonstrated as an effective method to tailor the properties of lasers. In general, SPs could be generated by the metal layer, such as Au or Ag, and transfer along the semiconductor–metal interface. Kao et al.[163] reduced the lasing threshold of perovskite by strong exciton–plasmon coupling between the Ag and perovskite films [Fig. 14(a)],[163] in which the confined optical fields between Ag and perovskite films could be enhanced about 19.3 and 7.7 times in comparison with bare perovskites and perovskites coated by Ag thin film, respectively. In 2017, Wang et al. deposited Al nanoparticles onto the surface of $CsPbBr_3$ perovskites. The lasing thresholds of $CsPbBr_3$ perovskite microrods were significantly reduced by >20%, and the output intensities were significantly enhanced via the plasmonic resonances.[172] In 2019, Wu et al. reported a method to enhance ASE performance of $MAPbI_3$ films by

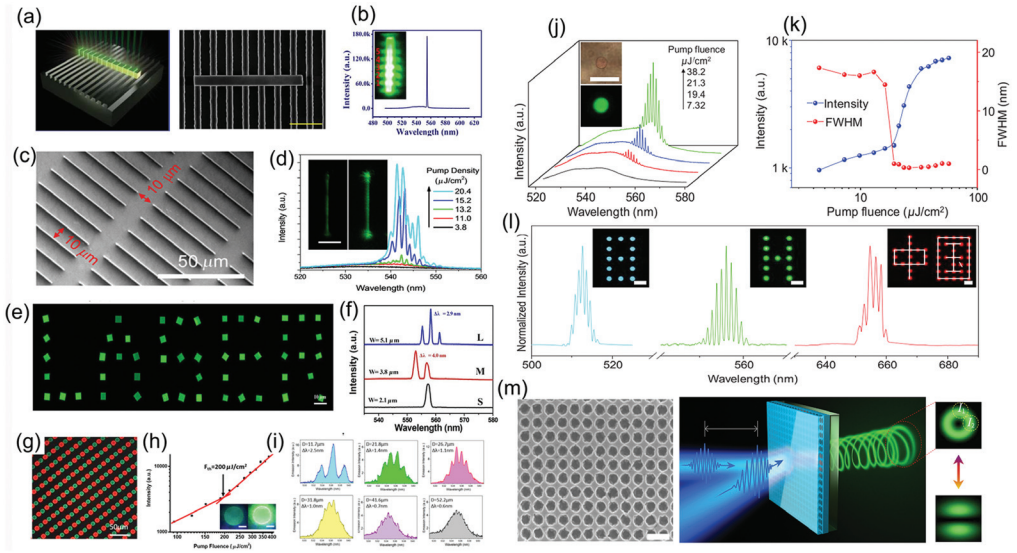

Fig. 13 (a) SEM image of the $MAPbBr_3$ microwire on silicon grating. Figures reproduced from Ref. 156. (b) Laser spectrum of $MAPbBr_3$ microwire. Figures reproduced from Ref. 156. (c) Optical image of $MAPbBr_3$ NW arrays. Figures reproduced from Ref. 157. (d) PL spectra of a single $MAPbBr_3$ NW under 400 nm laser. Figures reproduced from Ref. 157. (e) "LASER" patterned perovskite square MPs. Figures reproduced from Ref. 158. (f) Lasing spectra from perovskite MPs with different sizes. Figures reproduced from Ref. 158. (g) PL image of green and red QD arrays. Figures reproduced from Ref. 159. (h) Emission intensity versus excitation fluence measured from a $CsPbBr_3$ MD. Figures reproduced from Ref. 159. (i) Lasing spectra from $CsPbBr_3$ MDs with different diameters. Figures reproduced from Ref. 159. (j) PL spectra from a typical $MAPbBr_3$ MD with different power energies and (k) output intensity and FWHM as a function of pump intensity. Figures reproduced from Ref. 160. (l) Widely tunable lasing from $MAPbX_3$ arrays. Figures reproduced from Ref. 160. (m) Left: SEM image of the fabricated perovskite metasurface; right: ultrafast control of the quasi-BIC microlasers. Figures reproduced from Ref. 161.

adding Au NRs-doped PMMA on MA_3PbI_3 perovskite films. The ASE threshold was significantly reduced by ~36%, and the output intensity increased by 13.9-fold with the plasmon resonance enhancement of Au NRs.[173] Yang et al.[174] also reduced the lasing threshold of $CsPbBr_3$ perovskite nanocubes significantly by ~33% via the surface plasmonic effect of Au nanoparticles. In 2021, single-mode upconversion plasmonic lasing from $MAPbBr_3$ perovskite NCs was realized by Lu et al.,[164] exhibiting low threshold ~10 $\mu J/cm^2$ and small mode volume ~0.06 λ^3 at 6 K, where TiN was used as a promising resonance adjustable plasmonic platform [Fig. 14(b)]. Hsieh et al.[165] realized continuous-wave (CW) lasing from a single $CsPbBr_3$ QD in a plasmonic gap-mode nanocavity with low threshold of ~1.9 W/cm^2 and small mode volume of ~0.002λ^3 [Fig. 14(c)]. Most recently, Li et al.[166] proposed a hybrid nanocavity composed of $CsPbBr_3$ nanoparticles and a thin Au film, which could realize optically controlled quantum size effect by the reversible phase transition from polycrystalline to monocrystalline [Fig. 14(d)]. These results demonstrated that SPs could not only modulate the performance of perovskite lasers but also can realize deep subdiffraction plasmonic lasers.

Perovskite is also an ideal candidate to realize a room temperature exciton polariton laser, which mainly results from the strong exciton–photon coupling between the gain media and nanocavity. In perovskite laser researches, room temperature exciton polaritons have been realized with various nanostructures.[167,168,175,176] Perovskite NCs with self-assembled morphology can provide optical resonators due to the confinement of exciton–photon coupling. On the other hand, a planar optical cavity composed of two mirrors can be used as an F-P cavity conventionally. In 2018, Liu et al.[167] observed strong exciton–photon coupling in single $CsPbBr_3$ micro/NWs and $MAPbBr_3$ micro/NWs, respectively [Fig. 14(e)]. Moreover, polariton lasing was realized at room temperature with exceptionally large vacuum Rabi splitting of ~656 and 390 meV.[167,175] Shang et al.[176] proved light could propagate as an exciton–photon in $CsPbBr_3$ NWs at room temperature, increasing optical absorption and emission in comparison with bulk crystals. They demonstrated that the decrease of $CsPbBr_3$ dimensions could enhance the exciton–photon coupling strength, which increased the exciton fraction. Furthermore, they found that the increase of temperature could significantly decrease the exciton fraction of exciton–photons, causing high thresholds and restraining CW lasing above 100 K. They successfully realized CW-pumped lasing from $CsPbBr_3$ nanoribbons by reducing the height to ~120 nm on sapphires with low threshold of ~0.13 kW/cm^2 [Fig. 14(f)].[168] Then, they coupled $MAPbBr_3$ NWs with a hybrid plasmonic microcavity to enhance exciton–photon interaction.[177] They observed a Rabi-splitting up to ~564 meV in a hybrid perovskite/SiO_2/Ag waveguide microcavity at room temperature. In 2017, Su et al.[178] reported room-temperature polariton lasing based on an epitaxy-free all-inorganic $CsPbCl_3$ nanoplatelet embedded in DBRs,

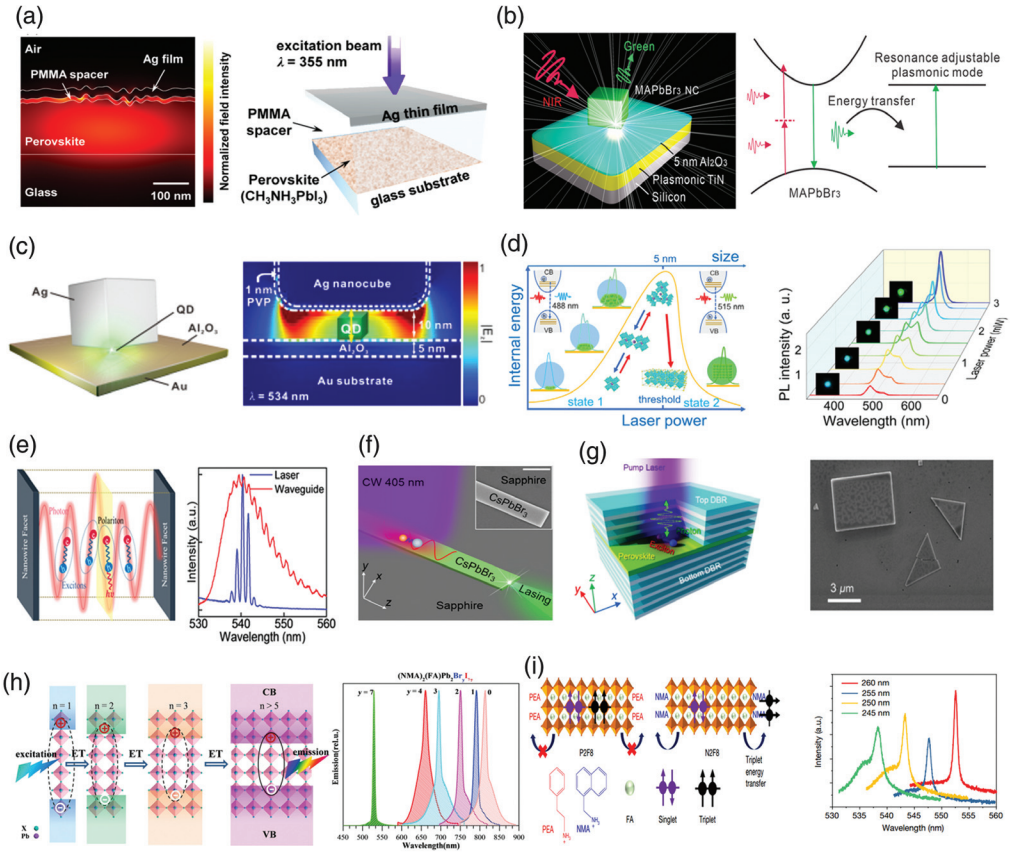

Fig. 14 (a) Field intensity distributions and schematic structure of Ag/PMMA/perovskite. Figures reproduced from Ref. 163. (b) Schematic and working process of plasmonic nanolaser of $MAPbBr_3/Al_2O_3/TiN$. Figures reproduced from Ref. 164. (c) Schematic and calculated electric field distribution of plasmonic nanolaser based on $CsPbBr_3$ QDs. Figures reproduced from Ref. 165. (d) Schematic of phase transition from polycrystalline to monocrystalline $CsPbBr_3$ nanoparticles by adjusting the laser power and the PL spectrum under different laser power. Figures reproduced from Ref. 166. (e) Schematic polaritons in a micro/NW cavity and lasing spectrum of $CsPbBr_3$ NWs. Figures reproduced from Ref. 167. (f) Schematic of CW lasing of $CsPbBr_3$ nanoribbons. Figures reproduced from Ref. 168. (g) Schematic structure of $CsPbBr_3$ flakes/DBR microcavity and SEM image of $CsPbBr_3$ flakes. Figures reproduced from Ref. 169. (h) Cascade energy transfer in quasi-2D perovskite and tunable ASE from solution-processed $(NMA)_2(FA)Pb_2Br_yI_{7-y}$ films. Figures reproduced from Ref. 170. (i) Chemical structures of quasi-2D perovskite with different organic cations and CW lasing characteristics of quasi-2D perovskite films. Figures reproduced from Ref. 171.

supporting F-P oscillations. The polariton lasing exhibited a threshold of ~12 $\mu J/cm^2$. Zhang et al.[169] investigated the trapping of polaritons in micron-sized $CsPbBr_3$ flakes embedded in DBRs as a microcavity [Fig. 14(g)]. They demonstrated quantized polariton states arising from the optical confinement of flakes.

In comparison with perovskite NCs with 3D structure, quasi-2D perovskites have a quantum well (QW) structure with the advantages of large exciton binding energy and low nonradiation loss and are more easily coupled with a resonant cavity. In 2018, Fieramosca et al. observed strong exciton–photon coupling from hybrid 2D perovskite flakes. The organic ligands efficiently affected the out-of-plane exciton–photon coupling, suggesting that the organic interlayer plays a significant role in the anisotropy of the exciton and exciton polariton.[179] Then, they observed highly interacting polaritons in $(PEA)_2PbI_4$ with an excitonic interaction constant as ~3 $\mu eV\,\mu m^2$, which was two orders higher than that of organic excitons.[180] Zhang et al.[181] investigated cavity polariton modes in 2D perovskite $(PEA)_2PbBr_4$ sheets. The perovskite layer naturally could act as an F-P cavity and exhibited evident cavity polariton modes with Rabi splitting energy of ~259 meV. Li et al.[170] first reported room temperature optical gain from 2D perovskite $(NMA)_2FA_{n-1}Pb_nX_{3n+1}$ ($NMA = C_{10}H_7CH_2NH_3^+$). In these layered perovskite nanostructures, multiple QW phases naturally form an energy cascade, enabling an ultrafast energy transfer process from higher energy bandgap QWs ($n < 5$) to lower energy bandgap QWs ($n > 5$). They obtained tunable ASE ranging from 530 to 810 nm with low ASE threshold (<20.0 $\mu J/cm^2$) [Fig. 14(h)]. Later, lasing based on these quasi-2D perovskite nanostructure has also been realized by researchers, e.g., Liang et al. investigated multicolor lasing from $(BA)_2(MA)_{n-1}$

Table 1 Lasing performance of perovskite.

Materials	Nanostructure	Laser mode	Emission wavelength	Threshold	Year	Ref.
$CsPbX_3$	QD on silica sphere	WGM	400 to 700 nm	5 to 22 $\mu J/cm^2$	2015	127
$CsPbBr_3$	$CsPbX_3/SiO_2$ composite	Random	520 to 530 nm	40 $\mu J/cm^2$	2017	131
$FAPbBr_3$	$FAPbX_3/SiO_2$	Random	540 nm	413.7 $\mu J/cm^2$	2020	136
$CsPbBr_3$	QD in silica sphere	Random/WGM	530 nm	430 $\mu J/cm^2$	2019	137
$CsPbBr_3$	QD in capillary tube	WGN	530 to 540 nm	11 $\mu J/cm^2$	2015	138
$CsPbBr_3$	QD in capillary tube	WGM	535 nm	0.9 mJ/cm^2	2016	139
$FAPbBr_3$	QD in capillary tube	WGM	540 to 550 nm	0.31 mJ/cm^2	2019	132
$CsPbBr_3$	DBR/$CsPbBr_3$QD/DBR	F-P	460 to 650 nm	9 $\mu J/cm^2$	2017	133
$CsPbBr_3$	DBR/$CsPbBr_3$QD/DBR	F-P	520 nm	0.39 $\mu J/cm^2$	2017	134
$FAPbBr_3$	Flexile DBR/$FAPbBr_3$ film/DBR	F-P	552.7 nm	18.3 $\mu J/cm^2$	2017	135
$MAPbBr_3$	DBR/$MAPbBr_3$ film/Ag	F-P	552 nm	421 $\mu J/cm^2$	2020	140
$MAPbX_3$	NWs	F-P	500 to 790 nm	0.22 $\mu J/cm^2$	2015	144
$MAPbX_3$	NWs	F-P	551, 750, 777 nm	11 $\mu J/cm^2$	2015	49
$CsPbX_3$	NWs and NPs	F-P	430, 532, 550 nm	5 $\mu J/cm^2$	2016	55
$CsPbX_3$	NWs	F-P	420 to 710 nm	6.2 $\mu J/cm^2$	2016	145
$CsPbX_3$	Micro/NRs	F-P	428 to 628 nm	14.1 $\mu J/cm^2$	2017	75
$CsPbCl_{3-3x}Br_{3x}$	NWs	F-P	480 to 525 nm	11.7 to 35.0 $\mu J/cm^2$	2020	146
$MAPbI_3$	NPs	WGM	780 nm	37 $\mu J/cm^2$	2014	80
$MAPbCl_xBr_{3-x}$	Microdisks	WGM	525 to 558 nm	3.6 $\mu J/cm^2$	2015	150
$MAPbI_3$	Microplatelets	WGM	780 nm	12 $\mu J/cm^2$	2016	151
$MAPbBr_3$	Microplates	WGM	550 nm	20 $\mu J/cm^2$	2017	152
$MAPbI_3$	Triangular nanoplatelets	WGM	780 nm	18.7 $\mu J/cm^2$	2019	148
$CsPbX_3$	Nanoplatelets	WGM	400 to 700 nm	2.0 to 10.0 $\mu J/cm^2$	2016	149
$CsPbI_3$	NSs	WGM	702 to 725 nm	0.3 mJ/cm^2	2018	86
$CsPb_2Br_5$	Microplates	F-P	530, 540 nm	230 $\mu J/cm^2$	2020	153
		WGM		180 $\mu J/cm^2$		
$CsPbX_3$	MSs	WGM	425 to 715 nm	0.42 $\mu J/cm^2$	2017	100
$CsPbBr_3$	MSs	WGM	520 to 542 nm	203.7 $\mu J/cm^2$	2018	154
$CsPbBr_3$	Nanocuboids	F-P	531 nm	40.2 $\mu J/cm^2$	2018	129
$MAPbBr_3$	Pyramids	F-P	530 nm	26 $\mu J/cm^2$	2018	102
$CsPbI_3$	Pyramids	F-P	720 nm	21.56 to 53.15 $\mu J/cm^2$	2019	103
$MAPbBr_3$	Microwire array	F-P	554 nm	5.9 $\mu J/cm^2$	2016	156
$MAPbX_3$	NW array	F-P	543 nm	12.3 $\mu J/cm^2$	2017	157
$MAPbX_3$	Microplate array	WGM	510 to 780 nm	3.5 $\mu J/cm^2$	2016	158
$CsPbX_3$	QDs array	WGM	534 nm	200 $\mu J/cm^2$	2018	159
$MAPbX_3$	Microdisk array	WGM	510 to 650 nm	21.3 $\mu J/cm^2$	2019	160
$CsPbBr_3$	$CsPbBr_3$ microrod/Al nanoparticle	SP	540 nm	7.24 $\mu J/cm^2$	2017	172
$CsPbBrI_3$	$CsPbBr_3$/PEDOT:PSS/Au nanoparticle	SP	542 nm	157.6 $\mu J/cm^2$	2018	174
$MAPbBr_3$	$MAPbBr_3/Al_2O_3/TiN$	SP	550 nm	10 $\mu J/cm^2$	2021	164
$CsPbBr_3$	$Ag/CsPbBr_3/Al_2O_3/Au$	SP	534 nm	1.9 W/cm^2	2021	165
$CsPbBr_3$	$CsPbBr_3$/Au	SP	495 to 520 nm	2.0 mW	2021	166
$CsPbBr_3$	NWs	F-P	520 nm	8 $\mu J/cm^2$	2018	167
$MAPbBr_3$	Micro/NWs	F-P	550 nm	15 $\mu J/cm^2$	2018	175
$CsPbBr_3$	Nanoribbons	F-P (CW lasing)	2.34 eV	0.13 kW/cm^2	2020	168
$CsPbCl_3$	DBR/$CsPbCl_3$/DBR	F-P	2.9 eV	12 $\mu J/cm^2$	2017	178

Materials	Nanostructure	Laser mode	Emission wavelength	Threshold	Year	Ref.
$CsPbBr_3$	DBR/$CsPbBr_3$/DBR	F-P	2.3 eV	0.25 $\mu J/cm^2$	2020	169
$(BA)_2(MA)_{n-1}Pb_nI_{3n+1}$	Quasi-2D perovskite flakes	F-P	630, 663, 687 nm	4.8 $\mu J/cm^2$	2019	182
$PEA_2A_{n-1}Pb_nBr_{3n+1}$ (A: MA, Cs)	UV glue/quasi-2D perovskite/glass	F-P	539 nm	10.5 $\mu J/cm^2$	2021	183
PEA-$FAPb_xBr_y$	Quasi-2D perovskite on DFB	CW lasing	553 nm	32.8 $\mu J/cm^2$	2020	171
NMA-$FAPb_xBr_y$			555 nm	4.7 $\mu J/cm^2$		

Pb_nI_{3n+1} ($BA = C_4H_9NH_3^+$) in 2019.[182] Most recently, Liu et al. shrank the quasi-2D perovskites laser to the deep-subwavelength scale with 50 nm, which was the smallest room temperature all-dielectric laser.[183] They revealed the contribution from excitons and polarons to the high optical gain, which provided an insight into the design of next-generation integrated laser sources. Qin et al.[171,184] found that the triplet excitons in hybrid quasi-2D perovskite have a lifetime up to 1 μs, which might cause the disappearance of the laser. Then, using a distributed-feedback (DFB) cavity with a high Q and triplet management strategies, they realized stable room-temperature CW lasing in quasi-2D perovskite films [Fig. 14(i)]. The representative works about perovskite lasers in recent years are summarized in Table 1. All of these progresses prove the potential of perovskite materials in micro/nanolasers.

4 Conclusion and Outlook

Over the last few years, tremendous investigations have been carried out on metal halide perovskite materials, especially studies of the corresponding physicochemical properties and exploration of relevant applications in optoelectronic devices. In this review, we summarized the recent developments of the synthesis strategies, the morphological control, and lasing application of metal halide perovskite materials. The various synthetic methods for the fabrication of perovskite NCs have been investigated in previous researches, including the solution method and chemical deposition method. Moreover, the morphology of perovskite NCs can be controlled with different dimensions via adjusting the reaction conditions. Their structure-related optical properties were investigated on the single-particle with various structures as 0D, 1D, 2D, and 3D, enabling their potential in LEDs, solar cells, photodetectors, and lasers.

In spite of the tremendous advances in perovskite materials and perovskite-based lasers so far, there are still many issues to be further solved. The central issue of perovskite materials is their instability, which is the biggest obstacle for their industrialization. Although enormous work has been performed to enhance the stability of perovskites, such as the surface ligand modification or encapsulation method, the instability characteristic of the perovskites still limits their commercial applications. So far, the mechanisms of their decomposition are not yet clearly understood, hindering their further performance improvements. Another important issue related to lead halide perovskite materials is the urgent trend of reducing or removing the lead element due to its toxicity. For this purpose, some strategies have been proposed to constitute lead-free perovskites by possible substitutes using either homovalent elements such as Sn and Ge or heterovalent elements such as Bi and Sb.[185,186] Unfortunately, the optoelectronic properties of lead-free perovskites have not been effectively improved. Furthermore, the nucleation and growth mechanisms of perovskite NCs are yet to be revealed clearly, which is helpful to accurately control the morphology of the perovskite NCs for better understanding structure–property relationships. Last, but not least, theoretical explanation about the photophysics of perovskite NCs is necessary to better explain the quantum size effects of perovskite crystals, which could guide the research directions to regulate and control their electronic, optical, and defect properties.

The potential of perovskite materials in laser applications has been abundantly demonstrated. We reviewed a variety of laser cavities and summarized the dependence between the resonant cavity and the structure of perovskite NCs. Various linear and nonlinear perovskite lasers with an ultralow threshold have been realized in single perovskite NCs with different dimensions. Owing to the large gain coefficient and long-distance ambipolar carrier-transport, perovskites have great potential in electrically driven lasers, which have huge application value in integrated optoelectronic devices. But until now, all of the obtained perovskite lasers are pumped by laser excitation. The research about electrically pumped perovskite lasers has not been realized. Further investigation of resonant cavities, together with further reduction of the lasing threshold under optical excitation via optimization of the material properties, will boost the realization for electrically driven lasers of perovskites. The future trend of the perovskite-based laser is to integrate with optoelectronic components for further waveguide and signal processing. More importantly, the resonance and gain of perovskite materials and perovskite-based lasers need photophysical theory, which will inspire exploring the carrier relaxation and charge transfer processes of high-performance devices.

Acknowledgments

This work was supported by the National Key R&D Program of China (2018YFB2200500, 2017YFE0123700), the National Natural Science Foundation of China (61975023, 61875211, 22072010, 61925507, 61905264, 62005296, and 92050203), the Strategic Priority Research Program of CAS (XDB16030400), CAS Interdisciplinary Innovation Team, Program of Shanghai Academic/Technology Research Leader (Grant No. 18XD1404200), China Postdoctoral Science Foundation (2020M681421), Chongqing Research Program of Basic Research and Frontier Technology (cstc2018jszx-cyzdX0137), the Natural Science Foundation of Chongqing (cstc2019jcyj-msxmX0522), and the Science and Technology Research Program of Chongqing Municipal Education Commission (KJQN201900515).

References

1. D. Weber, "$CH_3NH_3SnBr_xI_{3-x}(x = 0-3)$, a Sn(II)-system with cubic perovskite structure," *Zeitschrift Fur Naturforsch. Sect. B* **33**(8), 862–865 (1978).
2. D. Weber, "$CH_3NH_3PbX_3$, a Pb(II)-system with cubic perovskite structure," *Zeitschr. Naturforsch. Sect. B* **33**(12), 1443–1445 (1978).
3. D. Weber, "The Perovskite system $CH_3NH_3[Pb_nSn_{1-n}X_3]$ (X = C1, Br, I)," *Zeitschr. Naturforsch. Sect. B* **34**(7), 939–941 (1979).
4. A. Kojima et al., "Organometal halide perovskites as visible-light sensitizers for photovoltaic cells," *J. Am. Chem. Soc.* **131**(17), 6050–6051 (2009).
5. S. D. Stranks and H. J. Snaith, "Metal-halide perovskites for photovoltaic and light-emitting devices," *Nat. Nanotechnol.* **10**(5), 391–402 (2015).
6. R. Gottesman and A. Zaban, "Perovskites for photovoltaics in the spotlight: photoinduced physical changes and their implications," *Acc. Chem. Res.* **49**(2), 320–329 (2016).
7. Q. Lin et al., "Organohalide perovskites for solar energy conversion," *Acc. Chem. Res.* **49**(3), 545–553 (2016).
8. N. G. Park et al., "Towards stable and commercially available perovskite solar cells," *Nat. Energy* **3**(11), 16152 (2016).
9. J. Seo et al., "Rational strategies for efficient perovskite solar cells," *Acc. Chem. Res.* **49**(3), 562–572 (2016).
10. W. Zhang et al., "Metal halide perovskites for energy applications," *Nat. Energy* **3**(6), 16048 (2016).
11. P. Zhang et al., "Perovskite solar cells with ZnO electron-transporting materials," *Adv. Mater.* **30**(3), 1703737 (2018).
12. A. K. Jena et al., "Halide perovskite photovoltaics: background, status, and future prospects," *Chem. Rev.* **119**(5), 3036–3103 (2019).
13. M. Jung et al., "Perovskite precursor solution chemistry: from fundamentals to photovoltaic applications," *Chem. Soc. Rev.* **48**(7), 2011–2038 (2019).
14. M. Ahmadi et al., "A review on organic-inorganic halide perovskite photodetectors: device engineering and fundamental physics," *Adv. Mater.* **29**(41), 1605242 (2017).
15. F. P. G. de Arquer et al., "Solution-processed semiconductors for next-generation photodetectors," *Nat. Rev. Mater.* **2**(3), 16100 (2017).
16. W. Wang et al., "Research progress of perovskite materials in photocatalysis- and photovoltaics-related energy conversion and environmental treatment," *Chem. Soc. Rev.* **44**(15), 5371–5408 (2015).
17. K. Xiao et al., "All-perovskite tandem solar cells with 24.2% certified efficiency and area over 1 cm^2 using surface-anchoring zwitterionic antioxidant," *Nat. Energy* **5**(11), 870–880 (2020).
18. X. H. Luo et al., "Progress of all-perovskite tandem solar cells: the role of narrow-bandgap absorbers," *Sci. China-Chem.* **64**(2), 218–227 (2020).
19. R. Meitzner et al., "Agrivoltaics-the perfect fit for the future of organic photovoltaics," *Adv. Energy Mater.* **11**(1), 2002551 (2020).
20. T. Moot et al., "Choose your own adventure: fabrication of monolithic all-perovskite tandem photovoltaics," *Adv. Mater.* **32**(50), 2003312 (2020).
21. S. Kondo et al., "Photoluminescence and stimulated emission from microcrystalline $CsPbCl_3$ films prepared by amorphous-to-crystalline transformation," *Phys. Rev. B* **70**(20), 205322 (2004).
22. S. Kondo et al., "Confinement-enhanced stimulated emission in microcrystalline $CsPbCl_3$ films grown from the amorphous phase," *J. Cryst. Growth* **282**(1–2), 94–104 (2005).
23. G. C. Xing et al., "Low-temperature solution-processed wavelength-tunable perovskites for lasing," *Nat. Mater.* **13**(5), 476–480 (2014).
24. S. Kondo et al., "High intensity photoluminescence of microcrystalline $CsPbBr_3$ films: evidence for enhanced stimulated emission at room temperature," *Curr. Appl. Phys.* **7**(1), 1–5 (2007).
25. F. Zhang et al., "Brightly luminescent and color-tunable colloidal $CH_3NH_3PbX_3$ (X = Br, I, Cl) quantum dots: potential alternatives for display technology," *ACS Nano* **9**(4), 4533–4542 (2015).
26. V. Adinolfi et al., "The in-gap electronic state spectrum of methylammonium lead iodide single-crystal perovskites," *Adv. Mater.* **28**(17), 3406–3410 (2016).
27. W. Metaferia et al., "Gallium arsenide solar cells grown at rates exceeding 300 $\mu m\ h^{-1}$ by hydride vapor phase epitaxy," *Nat. Commun.* **10**(1), 3361 (2019).
28. X. P. Shen et al., "Improved air-stability of an organic-inorganic perovskite with anhydrously transferred graphene," *J. Mater. Chem. C* **6**(32), 8663–8669 (2018).
29. Y. Sun et al., "Long-term stability of organic-inorganic hybrid perovskite solar cells with high efficiency under high humidity conditions," *J. Mater. Chem. A* **5**(4), 1374–1379 (2017).
30. H. C. Yu et al., "Organic-inorganic perovskite plasmonic nanowire lasers with a low threshold and a good thermal stability," *Nanoscale* **8**(47), 19536–19540 (2016).
31. N. Wang et al., "Perovskite light-emitting diodes based on solution-processed self-organized multiple quantum wells," *Nat. Photonics* **10**(11), 699–704 (2016).
32. S. De Wolf et al., "Organometallic halide perovskites: sharp optical absorption edge and its relation to photovoltaic performance," *J. Phys. Chem. Lett.* **5**(6), 1035–1039 (2014).
33. D. Chen and X. Chen, "Luminescent perovskite quantum dots: synthesis, microstructures, optical properties and applications," *J. Mater. Chem. C* **7**(6), 1413–1446 (2019).
34. Y. Zhang et al., "Photonics and optoelectronics using nanostructured hybrid perovskite media and their optical cavities," *Phys. Rep.* **795**, 1–51 (2019).
35. H. Dong et al., "Materials chemistry and engineering in metal halide perovskite lasers," *Chem. Soc. Rev.* **49**(3), 951–982 (2020).
36. J. Xu et al., "Halide perovskites for nonlinear optics," *Adv. Mater.* **32**(3), 1806736 (2020).
37. Y. Bekenstein et al., "Highly luminescent colloidal nanoplates of perovskite cesium lead halide and their oriented assemblies," *J. Am. Chem. Soc.* **137**(51), 16008–16011 (2015).
38. H. Huang et al., "Colloidal lead halide perovskite nanocrystals: synthesis, optical properties and applications," *NPG Asia Mater.* **8**(11), e328 (2016).
39. X. M. Li et al., "$CsPbX_3$ quantum dots for lighting and displays: room-temperature synthesis, photoluminescence superiorities, underlying origins and white light-emitting diodes," *Adv. Funct. Mater.* **26**(15), 2435–2445 (2016).
40. Z. X. Liu et al., "Morphology-tailored halide perovskite platelets and wires: from synthesis, properties to optoelectronic devices," *Adv. Opt. Mater.* **6**(17), 1800413 (2018).
41. G. Nedelcu et al., "Fast anion-exchange in highly luminescent nanocrystals of cesium lead halide perovskites ($CsPbX_3$, X = Cl, Br, I)," *Nano Lett.* **15**(8), 5635–5640 (2015).
42. L. Protesescu et al., "Nanocrystals of cesium lead halide perovskites ($CsPbX_3$, X = Cl, Br, and I): novel optoelectronic materials showing bright emission with wide color gamut," *Nano Lett.* **15**(6), 3692–3696 (2015).
43. Y. X. Li et al., "Advances in metal halide perovskite nanocrystals: synthetic strategies, growth mechanisms, and optoelectronic applications," *Mater. Today* **32**, 204–221 (2020).
44. A. Fakharuddin et al., "Inorganic and layered perovskites for optoelectronic devices," *Adv. Mater.* **31**(47), 1807095 (2019).
45. C. Li et al., "Formability of ABX_3 (X = F, CI, Br, I) halide perovskites," *Acta Crystallogr. B* **B64**(6), 702–707 (2008).
46. Q. D. Sun and W. J. Yin, "Thermodynamic stability trend of cubic perovskites," *J. Am. Chem. Soc.* **139**(42), 14905–14908 (2017).
47. J. Shamsi et al., "Colloidal synthesis of quantum confined single crystal $CsPbBr_3$ nanosheets with lateral size control up to the micrometer range," *J. Am. Chem. Soc.* **138**(23), 7240–7243 (2016).

48. J. Cho et al., "Ligand-mediated modulation of layer thicknesses of perovskite methylammonium lead bromide nanoplatelets," *Chem. Mat.* **28**(19), 6909–6916 (2016).
49. J. Xing et al., "Vapor phase synthesis of organometal halide perovskite nanowires for tunable room-temperature nanolasers," *Nano Lett.* **15**(7), 4571–4577 (2015).
50. S. B. Sun et al., "Ligand-mediated synthesis of shape-controlled cesium lead halide perovskite nanocrystals via reprecipitation process at room temperature," *ACS Nano* **10**(3), 3648–3657 (2016).
51. D. D. Zhang et al., "Solution-phase synthesis of cesium lead halide perovskite nanowires," *J. Am. Chem. Soc.* **137**(29), 9230–9233 (2015).
52. J. K. Sun et al., "Polar solvent induced lattice distortion of cubic $CsPbI_3$ nanocubes and hierarchical self-assembly into orthorhombic single-crystalline nanowires," *J. Am. Chem. Soc.* **140**(37), 11705–11715 (2018).
53. D. D. Zhang et al., "Synthesis of composition tunable and highly luminescent cesium lead halide nanowires through anion-exchange reactions," *J. Am. Chem. Soc.* **138**(23), 7236–7239 (2016).
54. F. Di Stasio et al., "Reversible concentration-dependent photoluminescence quenching and change of emission color in $CsPbBr_3$ nanowires and nanoplatelets," *J. Phys. Chem. Lett.* **8**(12), 2725–2729 (2017).
55. S. W. Eaton et al., "Lasing in robust cesium lead halide perovskite nanowires," *Proc. Natl. Acad. Sci. U. S. A.* **113**(8), 1993–1998 (2016).
56. M. Imran et al., "Colloidal synthesis of strongly fluorescent $CsPbBr_3$ nanowires with width tunable down to the quantum confinement regime," *Chem. Mat.* **28**(18), 6450–6454 (2016).
57. Y. Liu et al., "Room temperature colloidal synthesis of $CsPbBr_3$ nanowires with tunable length, width and composition," *J. Mater. Chem. C* **6**(29), 7797–7802 (2018).
58. D. Amgar et al., "Tunable length and optical properties of $CsPbX_3$ (X = Cl, Br, I) nanowires with a few unit cells," *Nano Lett.* **17**(2), 1007–1013 (2017).
59. Z. Yuan et al., "A facile one-pot synthesis of deep blue luminescent lead bromide perovskite microdisks," *Chem. Commun.* **51**(91), 16385–16388 (2015).
60. V. K. Ravi et al., "Origin of the substitution mechanism for the binding of organic ligands on the surface of $CsPbBr_3$ perovskite nanocubes," *J. Phys. Chem. Lett.* **8**(20), 4988–4994 (2017).
61. J. A. Sichert et al., "Quantum size effect in organometal halide perovskite nanoplatelets," *Nano Lett.* **15**(10), 6521–6527 (2015).
62. J. Chen et al., "Vapor-phase epitaxial growth of aligned nanowire networks of cesium lead halide perovskites ($CsPbX_3$, X = Cl, Br, I)," *Nano Lett.* **17**(1), 460–466 (2017).
63. S. T. Ha et al., "Synthesis of organic-inorganic lead halide perovskite nanoplatelets: towards high-performance perovskite solar cells and optoelectronic devices," *Adv. Opt. Mater.* **2**(9), 838–844 (2014).
64. Z. X. Liu et al., "One-step vapor-phase synthesis and quantum-confined exciton in single-crystal platelets of hybrid halide perovskites," *J. Phys. Chem. Lett.* **10**(10), 2363–2371 (2019).
65. C. K. Lin et al., "Two-step patterning of scalable all-inorganic halide perovskite arrays," *ACS Nano* **14**(3), 3500–3508 (2020).
66. W. W. Chen et al., "Tunable photoluminescence of $CsPbBr_3$ perovskite quantum dots for light emitting diodes application," *J. Solid State Chem.* **255**, 115–120 (2017).
67. X. Fang et al., "Wide range tuning of the size and emission color of $CH_3NH_3PbBr_3$ quantum dots by surface ligands," *AIP Adv.* **7**(8), 085217 (2017).
68. R. K. Singh et al., "Structural, morphological and thermodynamic parameters investigation of tunable $MAPb_{1-x}Cd_xBr_{3-2x}I_{2x}$ hybrid perovskite," *J. Alloys Comp.* **866**, 158936 (2021).
69. S. R. Smock et al., "The surface chemistry and structure of colloidal lead halide perovskite nanocrystals," *Acc. Chem. Res.* **54**(3), 707–718 (2021).
70. Y. Xie et al., "Highly efficient blue-emitting $CsPbBr_3$ perovskite nanocrystals through neodymium doping," *Adv. Sci.* **7**(20), 2001698 (2020).
71. H. Deng et al., "Growth, patterning and alignment of organolead iodide perovskite nanowires for optoelectronic devices," *Nanoscale* **7**(9), 4163–4170 (2015).
72. D. D. Dong et al., "Bandgap tunable $Cs_x(CH_3NH_3)_{1-x}PbI_3$ perovskite nanowires by aqueous solution synthesis for optoelectronic devices," *Nanoscale* **9**(4), 1567–1574 (2017).
73. P. C. Zhu et al., "Direct conversion of perovskite thin films into nanowires with kinetic control for flexible optoelectronic devices," *Nano Lett.* **16**(2), 871–876 (2016).
74. J. He et al., "*In situ* synthesis and macroscale alignment of $CsPbBr_3$ perovskite nanorods in a polymer matrix," *Nanoscale* **10**(33), 15436–15441 (2018).
75. H. Zhou et al., "Vapor growth and tunable lasing of band gap engineered cesium lead halide perovskite micro/nanorods with triangular cross section," *ACS Nano* **11**(2), 1189–1195 (2017).
76. T. Qiu et al., "Recent advances in one-dimensional halide perovskites for optoelectronic applications," *Nanoscale* **10**(45), 20963–20989 (2018).
77. E. Z. Shi et al., "Two-dimensional halide perovskite nanomaterials and heterostructures," *Chem. Soc. Rev.* **47**(16), 6046–6072 (2018).
78. X. S. Tang et al., "Perovskite $CsPb_2Br_5$ microplate laser with enhanced stability and tunable properties," *Adv. Opt. Mater.* **5**(3), 1600788 (2017).
79. Z.-J. Li et al., "General strategy for the growth of $CsPbX_3$ (X = Cl, Br, I) perovskite nanosheets from the assembly of nanorods," *Chem. Mat.* **30**(11), 3854–3860 (2018).
80. Q. Zhang et al., "Room-temperature near-infrared high-Q perovskite whispering-gallery planar nanolasers," *Nano Lett.* **14**(10), 5995–6001 (2014).
81. X. Qin et al., "Perovskite photodetectors based on $CH_3NH_3PbI_3$ single crystals," *Chem.-Asian J.* **11**(19), 2675–2679 (2016).
82. A. Z. Pan et al., "Insight into the ligand-mediated synthesis of colloidal $CsPbBr_3$ perovskite nanocrystals: the role of organic acid, base, and cesium precursors," *ACS Nano* **10**(8), 7943–7954 (2016).
83. H. Huang et al., "Spontaneous crystallization of perovskite nanocrystals in nonpolar organic solvents: a versatile approach for their shape-controlled synthesis," *Angew. Chem.-Int. Ed.* **58**(46), 16558–16562 (2019).
84. J. Liu et al., "Two-dimensional $CH_3NH_3PbI_3$ perovskite: synthesis and optoelectronic application," *ACS Nano* **10**(3), 3536–3542 (2016).
85. C. Huo et al., "Field-effect transistors based on van-der-Waals-grown and dry-transferred all-inorganic perovskite ultrathin platelets," *J. Phys. Chem. Lett.* **8**(19), 4785–4792 (2017).
86. Z. Zheng et al., "Space-confined synthesis of 2D all-inorganic $CsPbI_3$ perovskite nanosheets for multiphoton-pumped lasing," *Adv. Opt. Mater.* **6**(22), 1800879 (2017).
87. N. F. Yu et al., "Light propagation with phase discontinuities: generalized laws of reflection and refraction," *Science* **334**(6054), 333–337 (2011).
88. X. J. Ni et al., "Broadband light bending with plasmonic nanoantennas," *Science* **335**(6067), 427–427 (2012).
89. B. Wang et al., "Visible-frequency dielectric metasurfaces for multiwavelength achromatic and highly dispersive holograms," *Nano Lett.* **16**(8), 5235–5240 (2016).
90. Y. B. Fan et al., "Resonance-enhanced three-photon luminescence via lead halide perovskite metasurfaces for optical encoding," *Nat. Commun.* **10**(1), 2085 (2019).
91. S. Sun et al., "All-dielectric full-color printing with TiO_2 metasurfaces," *ACS Nano* **11**(5), 4445–4452 (2017).
92. Y. S. Gao et al., "Nonlinear holographic all-dielectric metasurfaces," *Nano Lett.* **18**(12), 8054–8061 (2018).

93. H. L. Wang et al., "Nanoimprinted perovskite metasurface for enhanced photoluminescence," *Opt. Express* **25**(24), 1162–1171 (2017).
94. B. Jeong et al., "Polymer-assisted nanoimprinting for environment- and phase-stable perovskite nanopatterns," *ACS Nano* **14**(2), 1645–1655 (2020).
95. K. Y. Wang et al., "Micro- and nanostructured lead halide perovskites: from materials to integrations and devices," *Adv. Mater.* **33**(6), 2000306 (2021).
96. C. Zhang et al., "Lead halide perovskite-based dynamic metasurfaces," *Laser Photonics Rev.* **13**(7), 1900079 (2019).
97. B. Gholipour et al., "Organometallic perovskite metasurfaces," *Adv. Mater.* **29**(9), 1604268 (2017).
98. S. V. Makarov et al., "Multifold emission enhancement in nanoimprinted hybrid perovskite metasurfaces," *ACS Photonics* **4**(4), 728–735 (2017).
99. Z. P. Hu et al., "Robust cesium lead halide perovskite microcubes for frequency upconversion lasing," *Adv. Opt. Mater.* **5**(22), 1700419 (2017).
100. B. Tang et al., "Single-mode lasers based on cesium lead halide perovskite sub-micron spheres," *ACS Nano* **11**(11), 10681–10688 (2017).
101. Z. Wei et al., "Synthesis and encapsulation of all inorganic perovskite nanocrystals by microfluidics," *J. Mater. Sci.* **54**(9), 6841–6852 (2019).
102. Y. Mi et al., "Fabry–Perot oscillation and room temperature lasing in perovskite cube-corner pyramid cavities," *Small* **14**(9), 1703136 (2018).
103. L. Yang et al., "Temperature-dependent lasing of $CsPbI_3$ triangular pyramid," *J. Phys. Chem. Lett.* **10**(22), 7056–7061 (2019).
104. M. Chen et al., "Controlled growth of dodecapod-branched $CsPbBr_3$ nanocrystals and their application in white light emitting diodes," *Nano Energy* **53**, 559–566 (2018).
105. F. Li et al., "Controlled fabrication, lasing behavior and excitonic recombination dynamics in single crystal $CH_3NH_3PbBr_3$ perovskite cuboids," *Sci. Bull.* **64**(10), 698–704 (2019).
106. J. L. Xu et al., "Organized chromophoric assemblies for nonlinear optical materials: towards (sub)wavelength scale architectures," *Small* **11**(9–10), 1113–1129 (2015).
107. A. Autere et al., "Nonlinear optics with 2D layered materials," *Adv. Mater.* **30**(24), 1705963 (2018).
108. J. L. Xu et al., "Self-assembled organic microfibers for nonlinear optics," *Adv. Mater.* **25**(14), 2084–2089 (2013).
109. J. B. Xiong et al., "Wavelength dependent nonlinear optical response of tetraphenylethene aggregation-induced emission luminogens," *Mat. Chem. Front.* **2**(12), 2263–2271 (2018).
110. E. Garmire, "Nonlinear optics in daily life," *Opt. Express* **21**(25), 30532–30544 (2013).
111. B. B. Gu et al., "Molecular nonlinear optics: recent advances and applications," *Adv. Opt. Photonics* **8**(2), 328–369 (2016).
112. O. Tokel et al., "In-chip microstructures and photonic devices fabricated by nonlinear laser lithography deep inside silicon," *Nat. Photonics* **11**(10), 639 (2017).
113. S. H. Yue et al., "Multimodal nonlinear optical microscopy," *Laser Photonics Rev.* **5**(4), 496–512 (2011).
114. M. Savoini et al., "THz generation and detection by fluorenone based organic crystals," *ACS Photonics* **5**(3), 671–677 (2018).
115. H. Linnenbank et al., "Temperature dependent two-photon photoluminescence of $CH_3NH_3PbBr_3$: structural phase and exciton to free carrier transition," *Opt. Mater. Express* **8**(3), 511–521 (2018).
116. Y. Wang et al., "Nonlinear absorption and low-threshold multiphoton pumped stimulated emission from all-inorganic perovskite nanocrystals," *Nano Lett.* **16**(1), 448–453 (2016).
117. G. Walters et al., "Two-photon absorption in organometallic bromide perovskites," *ACS Nano* **9**(9), 9340–9346 (2015).
118. B. S. Kalanoor et al., "Third-order optical nonlinearities in organometallic methylammonium lead iodide perovskite thin films," *ACS Photonics* **3**(3), 361–370 (2016).
119. R. A. Ganeev et al., "Strong nonlinear absorption in perovskite films," *Opt. Mater. Express* **8**(6), 1472–1483 (2018).
120. J. Zhang et al., "Thickness-dependent nonlinear optical properties of $CsPbBr_3$ perovskite nanosheets," *Opt. Lett.* **42**(17), 3371–3374 (2017).
121. K. N. Krishnakanth et al., "Broadband femtosecond nonlinear optical properties of $CsPbBr_3$ perovskite nanocrystals," *Opt. Lett.* **43**(3), 603–606 (2018).
122. Q. Wei et al., "Recent progress in metal halide perovskite micro- and nanolasers," *Adv. Opt. Mater.* **7**(17), 1900080 (2019).
123. F. Hide et al., "Semiconducting polymers: a new class of solid-state laser materials," *Science* **273**(5283), 1833–1836 (1996).
124. B. R. Sutherland et al., "Perovskite thin films via atomic layer deposition," *Adv. Mater.* **27**(1), 53–58 (2015).
125. Q. Liao et al., "Tunable halide perovskites for miniaturized solid-state laser applications," *Adv. Opt. Mater.* **7**(17), 1900099 (2019).
126. Q. Zhang et al., "Advances in small perovskite-based lasers," *Small Methods* **3**(9), 1700163 (2017).
127. S. Yakunin et al., "Low-threshold amplified spontaneous emission and lasing from colloidal nanocrystals of caesium lead halide perovskites," *Nat. Commun.* **6**(1), 8056 (2015).
128. B. R. Sutherland et al., "Conformal organohalide perovskites enable lasing on spherical resonators," *ACS Nano* **8**(10), 10947–10952 (2014).
129. Z. Liu et al., "Robust subwavelength single-mode perovskite nanocuboid laser," *ACS Nano* **12**(6), 5923–5931 (2018).
130. C. Zhao et al., "Stable two-photon pumped amplified spontaneous emission from millimeter-sized $CsPbBr_3$ single crystals," *J. Phys. Chem. Lett.* **10**(10), 2357–2362 (2019).
131. X. M. Li et al., "Amino-mediated anchoring perovskite quantum dots for stable and low-threshold random lasing," *Adv. Mater.* **29**(36), 1701185 (2017).
132. Z. Z. Liu et al., "Two-photon pumped amplified spontaneous emission and lasing from formamidinium lead bromine nanocrystals," *ACS Photonics* **6**(12), 3150–3158 (2019).
133. Y. Wang et al., "Solution-processed low threshold vertical cavity surface emitting lasers from all-inorganic perovskite nanocrystals," *Adv. Funct. Mater.* **27**(13), 1605088 (2017).
134. C. Y. Huang et al., "$CsPbBr_3$ perovskite quantum dot vertical cavity lasers with low threshold and high stability," *ACS Photonics* **4**(9), 2281–2289 (2017).
135. S. Chen and A. Nurmikko, "Stable green perovskite vertical-cavity surface-emitting lasers on rigid and flexible substrates," *ACS Photonics* **4**(10), 2486–2494 (2017).
136. J. Yang et al., "High efficiency up-conversion random lasing from formamidinium lead bromide/amino-mediated silica spheres composites," *Adv. Opt. Mater.* **8**(12), 2000290 (2020).
137. Z. Liu et al., "Stable and enhanced frequency up-converted lasing from $CsPbBr_3$ quantum dots embedded in silica sphere," *Opt. Express* **27**(7), 9459–9466 (2019).
138. Y. Wang et al., "All-inorganic colloidal perovskite quantum dots: a new class of lasing materials with favorable characteristics," *Adv. Mater.* **27**(44), 7101–7108 (2015).
139. Y. Q. Xu et al., "Two-photon-pumped perovskite semiconductor nanocrystal lasers," *J. Am. Chem. Soc.* **138**(11), 3761–3768 (2016).
140. X. Li et al., "Two-photon-pumped high-quality, single-mode vertical cavity lasing based on perovskite monocrystalline films," *Nano Energy* **68**, 104334 (2020).
141. Z. Liu et al., "Advances in inorganic and hybrid perovskites for miniaturized lasers," *Nanophotonics* **9**(8), 2251–2272 (2020).
142. A. S. Polushkin et al., "Single-particle perovskite lasers: from material properties to cavity design," *Nanophotonics* **9**(3), 599–610 (2020).
143. Z. Liu et al., "Research progress of low-dimensional metal halide perovskites for lasing applications," *Chin. Phys. B* **27**(11), 114209 (2018).

144. H. M. Zhu et al., "Lead halide perovskite nanowire lasers with low lasing thresholds and high quality factors," *Nat. Mater.* **14**(6), 636–642 (2015).
145. Y. P. Fu et al., "Broad wavelength tunable robust lasing from single-crystal nanowires of cesium lead halide perovskites ($CsPbX_3$, X = Cl, Br, I)," *ACS Nano* **10**(8), 7963–7972 (2016).
146. B. Tang et al., "Energy transfer and wavelength tunable lasing of single perovskite alloy nanowire," *Nano Energy* **71**, 104641 (2020).
147. X. Wang et al., "Cesium lead halide perovskite triangular nanorods as high-gain medium and effective cavities for multiphoton-pumped lasing," *Nano Res.* **10**(10), 3385–3395 (2017).
148. G. Li et al., "Record-low-threshold lasers based on atomically smooth triangular nanoplatelet perovskite," *Adv. Funct. Mater.* **29**(2), 1805553 (2019).
149. Q. Zhang et al., "High-quality whispering-gallery-mode lasing from cesium lead halide perovskite nanoplatelets," *Adv. Funct. Mater.* **26**(34), 6238–6245 (2016).
150. Q. Liao et al., "Perovskite microdisk microlasers self-assembled from solution," *Adv. Mater.* **27**(22), 3405–3410 (2015).
151. X. F. Liu et al., "Periodic organic-inorganic halide perovskite microplatelet arrays on silicon substrates for room-temperature lasing," *Adv. Sci.* **3**(11), 1600137 (2016).
152. Q. Wei et al., "Two-photon optical properties in individual organic-inorganic perovskite microplates," *Adv. Opt. Mater.* **5**(24), 1700809 (2017).
153. Z. Z. Liu et al., "Mode selection and high-quality upconversion lasing from perovskite $CsPb_2Br_5$ microplates," *Photon. Res.* **8**(9), A31–A38 (2020).
154. B. Tang et al., "Ultrahigh quality upconverted single-mode lasing in cesium lead bromide spherical microcavity," *Adv. Opt. Mater.* **6**(20), 1800391 (2018).
155. B. Zhou et al., "Linearly polarized lasing based on coupled perovskite microspheres," *Nanoscale* **12**(10), 5805–5811 (2020).
156. K. Y. Wang et al., "High-density and uniform lead halide perovskite nanolaser array on silicon," *J. Phys. Chem. Lett.* **7**(13), 2549–2555 (2016).
157. P. Liu et al., "Organic–inorganic hybrid perovskite nanowire laser arrays," *ACS Nano* **11**(6), 5766–5773 (2017).
158. J. Feng et al., "'Liquid knife' to fabricate patterning single-crystalline perovskite microplates toward high-performance laser arrays," *Adv. Mater.* **28**(19), 3732–3741 (2016).
159. C. H. Lin et al., "Large-area lasing and multicolor perovskite quantum dot patterns," *Adv. Opt. Mater.* **6**(16), 1800474 (2018).
160. K. Wang et al., "Wettability-guided screen printing of perovskite microlaser arrays for current-driven displays," *Adv. Mater.* **32**(29), 2001999 (2020).
161. C. Huang et al., "Ultrafast control of vortex microlasers," *Science* **367**(6481), 1018–1021 (2020).
162. C. Li et al., "Surface-plasmon-assisted metal halide perovskite small lasers," *Adv. Opt. Mater.* **7**(17), 1900279 (2019).
163. T. S. Kao et al., "Localized surface plasmon for enhanced lasing performance in solution-processed perovskites," *Opt. Express* **24**(18), 20696–20702 (2016).
164. Y.-J. Lu et al., "Upconversion plasmonic lasing from an organo-lead trihalide perovskite nanocrystal with low threshold," *ACS Photonics* **8**(1), 335–342 (2020).
165. Y. H. Hsieh et al., "Perovskite quantum dot lasing in a gap-plasmon nanocavity with ultralow threshold," *ACS Nano* **14**(9), 11670–11676 (2020).
166. S. Li et al., "Optically-controlled quantum size effect in a hybrid nanocavity composed of a perovskite nanoparticle and a thin gold film," *Laser Photonics Rev.* **15**(3), 2000480 (2021).
167. W. Du et al., "Strong exciton–photon coupling and lasing behavior in all-inorganic $CsPbBr_3$ micro/nanowire Fabry-Pérot cavity," *ACS Photonics* **5**(5), 2051–2059 (2018).
168. Q. Shang et al., "Role of the exciton-polariton in a continuous-wave optically pumped $CsPbBr_3$ perovskite laser," *Nano Lett.* **20**(9), 6636–6643 (2020).
169. S. Zhang et al., "Trapped exciton–polariton condensate by spatial confinement in a perovskite microcavity," *ACS Photonics* **7**(2), 327–337 (2020).
170. M. Li et al., "Amplified spontaneous emission based on 2D Ruddlesden-Popper perovskites," *Adv. Funct. Mater.* **28**(17), 1707006 (2018).
171. C. Qin et al., "Stable room-temperature continuous-wave lasing in quasi-2D perovskite films," *Nature* **585**(7823), 53–57 (2020).
172. S. Wang et al., "Maskless fabrication of aluminum nanoparticles for plasmonic enhancement of lead halide perovskite lasers," *Adv. Opt. Mater.* **5**(21), 1700529 (2017).
173. X. Wu et al., "Highly stable enhanced near-infrared amplified spontaneous emission in solution-processed perovskite films by employing polymer and gold nanorods," *Nanoscale* **11**(4), 1959–1967 (2019).
174. J. Yang et al., "Enhanced single-mode lasers of all-inorganic perovskite nanocube by localized surface plasmonic effect from Au nanoparticles," *J. Luminesc.* **208**, 402–407 (2019).
175. S. Zhang et al., "Strong exciton-photon coupling in hybrid inorganic-organic perovskite micro/nanowires," *Adv. Opt. Mater.* **6**(2), 1701032 (2018).
176. Q. Shang et al., "Enhanced optical absorption and slowed light of reduced-dimensional $CsPbBr_3$ nanowire crystal by exciton-polariton," *Nano Lett.* **20**(2), 1023–1032 (2020).
177. Q. Shang et al., "Surface plasmon enhanced strong exciton-photon coupling in hybrid inorganic-organic perovskite nanowires," *Nano Lett.* **18**(6), 3335–3343 (2018).
178. R. Su et al., "Room-temperature polariton lasing in all-inorganic perovskite nanoplatelets," *Nano Lett.* **17**(6), 3982–3988 (2017).
179. A. Fieramosca et al., "Tunable out-of-plane excitons in 2D single-crystal perovskites," *ACS Photonics* **5**(10), 4179–4185 (2018).
180. A. Fieramosca et al., "Two-dimensional hybrid perovskites sustaining strong polariton interactions at room temperature," *Sci. Adv.* **5**(5), eaav9967 (2019).
181. X. Zhang et al., "Exciton-polariton properties in planar microcavity of millimeter-sized two-dimensional perovskite sheet," *ACS Appl. Mater. Interfaces* **12**(4), 5081–5089 (2020).
182. Y. Liang et al., "Lasing from mechanically exfoliated 2D homologous Ruddlesden–Popper perovskite engineered by inorganic layer thickness," *Adv. Mater.* **31**(39), 1903030 (2019).
183. Z. Liu et al., "Subwavelength-polarized quasi-two-dimensional perovskite single-mode nanolaser," *ACS Nano* **15**(4), 6900–6908 (2021).
184. C. Qin et al., "Triplet management for efficient perovskite light-emitting diodes," *Nat. Photonics* **14**(2), 70–75 (2020).
185. G. C. Xing et al., "Solution-processed tin-based perovskite for near-infrared lasing," *Adv. Mater.* **28**(37), 8191–8196 (2016).
186. Z. Y. Wu et al., "Room-temperature near-infrared random lasing with tin-based perovskites prepared by CVD processing," *J. Phys. Chem. C* **125**(9), 5180–5184 (2021).

Zhiping Hu is associate research fellow at Hangzhou Institute for Advanced Study, University of Chinese Academy of Sciences. She received her PhD degree from Chongqing University in 2018. From 2018 to 2020, she worked as a postdoctoral fellow at Peking University. Her current research focuses on the preparation and optical properties of luminescent materials and micro laser.

Zhengzheng Liu is a postdoctoral fellow at Shanghai Institute of Optics and Fine Mechanics (SIOM), Chinese Academy of Sciences (CAS). He received his PhD from SIOM in 2019. His current research interest is focused on the interaction between ultrashort pulsed laser and functional materials and the mechanism and devices of micro-nano lasers.

Zijun Zhan is a laboratory technician at the Hangzhou Institute for Advanced Study, University of Chinese Academy of Sciences. He received his BS and MS degrees in physics from Shandong Normal

University in 2013 and 2020, respectively. His current research interest is focused on the study of light–matter interaction and the fabrication of electroluminescent devices in perovskite materials.

Tongchao Shi is a PhD candidate at Shanghai Institute of Optics and Fine Mechanics, Chinese Academy of Sciences, China. He received his BS degree in optoelectronic information and engineering at Shandong University with honors in 2016. His current research interest is laser–matter interaction and ultrafast photogenerated carrier dynamics in polymer solar cells and perovskite.

Juan Du is a professor at Shanghai Institute of Optics and Fine Mechanics (SIOM), Chinese Academy of Sciences. She received her PhD from SIOM in 2007, then worked as a postdoc at the Advanced Ultrafast Laser Center of Nihon Electro-Communication University from 2007 to 2010. From 2013, she worked as a research fellow at SIOM. She has been engaged in the research of functional materials mechanism and the development of corresponding micro-nano devices.

Xiaosheng Tang is a professor at Chongqing University of Posts and Telecommunications. He received his PhD from National University of Singapore in 2013. Then he worked as a postdoc at Nanyang Technological University. He was professor at Chongqing University and from 2014 to 2020. His research is mainly focused on the synthesis of I-III-VI semiconductor quantum dots, perovskite quantum dots, the design and application of QLED, solar cells, and micro laser.

Yuxin Leng is laboratory chief of the State Key Laboratory of High Field Laser Physics at SIOM. He received his PhD from Shanghai Institute of Optics and Fine Mechanics, Chinese Academy of Sciences, in 2002. After that, he stayed at SIOM and became a professor in 2005. His research is focused on the development and application of ultra-intense and ultra-fast laser, nonlinear optics, and wavelength-tunable short-pulse laser and its interaction with materials.